Fracturing process of micro-concrete under uniaxial and triaxial compression: Insights from in-situ X-ray mechanical tests

O. Stamati, Emmanuel Roubin, E. Andò, Y. Malecot, P. Charrier

Version of Record: https://www.sciencedirect.com/science/article/pii/S0008884621002271
Manuscript_cffced6f9e3d9256da869a62d91bc640

Fracturing process of micro-concrete under uniaxial and triaxial compression: insights from *in-situ* x-ray mechanical tests

O. Stamati[a], E. Roubin[a], E. Andò[a], Y. Malecot[a], P. Charrier[a]

[a] *Univ. Grenoble Alpes, CNRS, Grenoble INP, 3SR, F-38000 Grenoble, France*

Abstract

This paper presents an experimental study of concrete at meso-scale (aggregates, macro-pores and mortar matrix) in order to get a better understanding of the local failure mechanisms known to drive the macroscopic mechanical behaviour of the material. The main originality comes from conducting *in-situ* x-ray mechanical tests on micro-concrete samples of realistic composition (including cement, sand, aggregates and water), under uniaxial compression and, for the first time, under triaxial compression at 5 MPa, 10 MPa and 15 MPa confining pressures. A timeseries analysis of the set of 3D images coming from each test allows for the measurement of the 3D kinematic fields (displacement and strain fields) throughout the experiments. The different failure patterns observed for each loading path are discussed, along with a quantification of the 3D fracturing processes at the scale of the largest heterogeneities (aggregates and macro-pores). With an increasing level of confinement, the transition from brittle to ductile response is observed, as well as an increase of the strength of the material. The pronounced impact of the meso-scale heterogeneities of concrete on their local failure mechanisms is highlighted. It is shown that strain localisation mainly originates between aggregates and mortar matrix, with the shape and location of the largest aggregates and macro-pores essentially driving the propagation of the cracking network.

Keywords: Meso-scale, Concrete, Local failure mechanisms, Fracture process, Uniaxial Compression, Triaxial Compression, *In-situ* x-ray tests, Digital Volume Correlation

1. Introduction

Over the years conventional tests have been extensively used to study the mechanical behaviour of concrete under multiaxial loading conditions. However, these kind of tests only provide overall material properties, with measurements of load and displacements often being insufficient to describe the complex heterogeneous stress/strain fields that arise during the quasi-brittle response of the material. It is however well known that the quasi-brittle response of concrete at the macro-scale is strongly influenced by the morphology and the properties of its material constituents and their mutual interactions over a large range of different length scales: from nano- to meso-scale, referring to nm (hydrated cement scale) and cm (largest aggregates scale), respectively [Mehta (1986); Weerheijm (2013); Basheer et al. (2005)].

Among these observation scales, the meso-scale is considered as a key scale for studying the influence of the heterogeneities on the macroscopic mechanical behaviour [Kim and Al-Rub (2011); Wriggers and Moftah (2006); Häfner et al. (2006)] and it is thus the scale at which this work focuses. At this scale, the presence of both aggregates and macro-pores, with various sizes and shapes in the concrete mix, results in an heterogeneous stress field,

even under uniform loading, leading to stress concentrations and initial micro-cracking around the weakest regions (usually the interfaces). With increasing load, these micro-cracks grow and coalesce into one (or several) critical macro-crack(s) resulting to the macroscopic failure of the material.

Towards investigating the role of these heterogeneities and thus improving the understanding of the complex fracture processes in concrete, non-destructive testing techniques offer new experimental possibilities. Scanning electron microscopy (SEM) [Mindess and Diamond (1980); Nemati (1997); Balendran et al. (1998); Chabaat et al. (2007)], acoustic emission (AE) [Anay et al. (2018)], ultrasonic methods [Aggelis and Philippidis (2004)] and digital speckle pattern interferometry (DSPI) [Jia and Shah (1994)] are some examples of such techniques. Among them, x-ray tomography is extremely well suited for studying fracture in concrete, providing the ability to conduct *in-situ* mechanical tests. These are the type of tests performed in this study.

The main advantage of performing such tests is that, apart from obtaining the typical macroscopic responses (such as force-displacement curves), the evolution of the 3D internal structure of the material from the intact (before loading) until the damaged (after unloading) state is followed and quantified. The rich experimental data coming from *in-situ* tests offer the opportunity for a direct comparison between experiments and simulations. By introducing the morphology obtained from the intact scan to the considered numerical model, crucial questions regarding the validation and the predictive ability of the latter can be addressed [Yang et al. (2017); Nitka and Tejchman (2018); Yu et al. (2018); Suchorzewski et al. (2017); Huang et al. (2015)]. A numerical model validated against experimental results coming from *in-situ* tests can provide thus promising potentials for a global statistical analysis.

However, due to the supplementary constrains imposed by the use of x-rays, these *in-situ* tests differ from the standard ones, both in terms of the specimen size (which has to be significantly smaller) and in terms of the instrumentation, since specific experimental facilities are required. Consequently, studies which involve *in-situ* experiments in cement-based materials are less common in literature. An exhaustive review of previous works concerning the use of x-ray tomography to characterise cementitious materials can be found in Brisard et al. (2020).

Among all the studies mentioned in Brisard et al. (2020), very few present *in-situ* mechanical tests. To mention some, Landis et al. (1999) and Landis et al. (2007) performed *in-situ* compression tests on small mortar specimens to study the 3D internal crack growth during loading. Mao et al. (2019) studied the damage and failure mechanisms of a circularly cylindrical concrete specimen under uniaxial compression, revealing regions of strain localisation and their evolution. Chateau et al. (2018) extracted the complex network of micro-cracks that progressively developed in a lightweight concrete sample subjected to uniaxial compression. Hurley and Pagan (2019) presented a combination of *in-situ* x-ray tomography and 3D x-ray diffraction to study the fracture network growth and the evolution of aggregate stress tensors of a $1\,\mathrm{mm}^3$ concrete cube (made of Portland cement and single-crystal quartz aggregates) during a uniaxial compression test. It is thus observed that the rare *in-situ* mechanical tests carried out on mortar or concrete in literature are mainly simple compression tests.

In a previous work of the authors [Stamati et al. (2019)], the fracturing process of concrete was studied under uniaxial tension, providing direct insights into the fundamental mechanisms of concrete fracture in mode I. However, the behaviour of concrete under confined compression is of major importance when it comes to investigate the mechan-

ical response of the material in structural applications, involving massive constructions or prestressed concrete structures. Previous experimental studies on triaxial behaviour of concrete have revealed the transition from brittle to ductile response, as well as the evolution in limit states and the modification of failure patterns with increasing confining pressure [Sfer et al. (2002); Gabet et al. (2008); Poinard et al. (2010); Zingg et al. (2016)]. The role of coarse aggregate composition, as well as the role of porosity on these observations were also studied [Piotrowska et al. (2014); Zingg et al. (2016)].

However, all these results only concerned macroscopic measurements. Coupled with x-ray tomography, Poinard et al. (2012) performed *ex-situ* triaxial compression tests to investigate the fracture network growth of concrete specimens. An important limitation of these tests is that the specimen needs to be unloaded and then removed from the loading frame in order to be scanned. Therefore, it is not possible to know the strain field and the crack patterns before unloading.

To the best of the authors knowledge, there is no study in literature concerning triaxial behaviour of concrete using *in-situ* experiments. The rich experimental data coming from such tests give direct access to the 3D kinematic fields during the test, providing a valuable quantification of the initiation and evolution of the strain localisation. Consequently, the *in-situ* triaxial compression tests on concrete constitute a very original aspect of the presented study.

This paper presents an experimental study at the meso-scale of the fracturing process of concrete under compressive triaxial loading. First (Section 2.1), the studied material is introduced, detailing the factors that determine the scale and morphology of the characteristic sample tested. The experimental set-up is then presented (Section 2.2), with a description of the testing procedure and the conducted experimental campaign (Section 2.3). In total 6 *in-situ* tests are conducted; 3 uniaxial compression tests and 3 triaxial compression tests at 5 MPa, 10 MPa and 15 MPa confining pressures. The methodology to analyse the acquired 3D images is then described (Section 2.4). First the technical challenge of separating the different phases of concrete's meso-structure is addressed and then the approach to quantify the evolution of the identified meso-structure during the loading is presented. The macroscopic results are discussed in Section 3.1, followed by a detailed description of the measured 3D kinematic fields for selected tests. Finally, the observed failure patterns coming from selected tests are presented in Section 3.2.

2. Materials and methods

The principal objective of this work is to study the mechanical behaviour of concrete at the meso-scale with a particular interest in the evolution of the failure mechanisms. This section presents the choices made concerning the studied material, as well as the experimental set-up and the image analysis methods that have been developed.

2.1. Studied material and sample preparation

It is usually accepted that for a given material, a ratio of at least equal to 5 is necessary between the size of a REV and the one of the largest heterogeneity. However, the objective here is to evaluate the impact of both the mechanical and the morphological properties of each phase (aggregates, macro-pores, mortar) on the local failure mechanisms and the macroscopic mechanical response of the material. Such an objective requires samples with rather small dimensions compared to the size of the largest heterogeneities, leading to choose a ratio approximately equal to 3 (*i.e.*, about 2 times smaller than the typical one). Apart from satisfying the above objective, the use of x-ray tomography combined with

a mechanical loading system imposes certain size constrains on the selected specimens. Making a trade-off between the different constraints (*i.e.*, required field of view, spatial resolution, loading system capacity), cylindrical micro-concrete [1] specimens are chosen of 11 mm in diameter and 22 mm in height.

A regular concrete mix is prepared, using ordinary Portland cement (CPA-52.5/CEM I), fine sand (D=1800 µm), aggregates (D=4 mm) and water. The mix proportion is 1 : 3 : 3.8 : 0.6[2], corresponding to an ordinary concrete in terms of both strength and slump (*i.e.*, workability). Except for the coarse aggregates size, this composition is the same as the one of a reference concrete (R30A7) which was exhaustively studied under triaxial loading in previous works [Gabet et al. (2008); Vu et al. (2009); Poinard et al. (2012)]. The aggregates used are rolled and siliceous (chemical composition: $SiO_2 > 97.3\%$) coming from Mios (France), with a maximum size of 4 mm (about the third of the specimen diameter). As explained above, this value is both large enough to create some discrepancy between different specimens, but also small enough to have a behaviour that is still representative of concrete (and compatible with the ASTM (2003) standard).

The choice to test small specimens of concrete implies that their preparation differs from the ordinary standard concrete specimens, adding some technical difficulties. As a first step, the material is mixed with a benchtop rotary mixer, then cast into cylindrical moulds of about 10 cm^3 in volume and cured in wet conditions for three days. By the end of this period, the concrete cylinders are removed from their moulds and stored for 28 days in a container filled with water saturated with lime to avoid any calcium hydroxide leaching out of concrete that would reduce its strength. A diamond instrumented core bit of 16 mm external and 11 mm internal diameter is used to extract cylindrical specimens from the material block. The cylindrical core is then cut to a nominal 23 mm length with a diamond wire saw, leaving an additional 1 mm margin. As a last step, both surfaces are rectified, resulting in a specimen that can be tested (shown in Fig.1a).

2.2. Test set-up

Laboratoire 3SR (Grenoble, France) hosts a specialised laboratory tomograph built by RX-Solutions (Annecy, France), the main components of which are the x-ray source, the rotation stage and the x-ray detector. In this type of set-up, shown in Fig. 1b, the source and the detector are kept fixed in space, while the specimen is rotated. A loading frame, shown in Fig. 1a, compatible with this scanner is used, allowing the specimens to be scanned while they are subjected to different loading paths.

As stated in the introduction, uniaxial and triaxial compression tests are performed in this study. A uniaxial compression test implies that a compressive axial force is applied to the specimen. In case of a triaxial test, the specimen is first subjected to an isotropic compression up to the desired confining pressure: $\sigma_1 = \sigma_2 = \sigma_3$. Thereafter, the specimen is axially compressed by applying deviatoric loading, which means that σ_1 is increased, while $\sigma_2 = \sigma_3$ remains constant and equal to the cell pressure.

Regardless of the stress path, the compressive axial force is applied on the bottom surface of the specimen by a ram, made of a steel cylinder of 10 mm in diameter (label No. 6 in Fig. 1a). An HBM C2-10 kN force meter (load capacity of 10 kN, label No. 8 in Fig. 1a) is used to measure the applied load, which is installed onto the loading head. An

[1] Concrete with a maximum aggregate size (*i.e.*, D_{max}) of a few millimeters.

[2] By weight of cement: sand: aggregates: water.

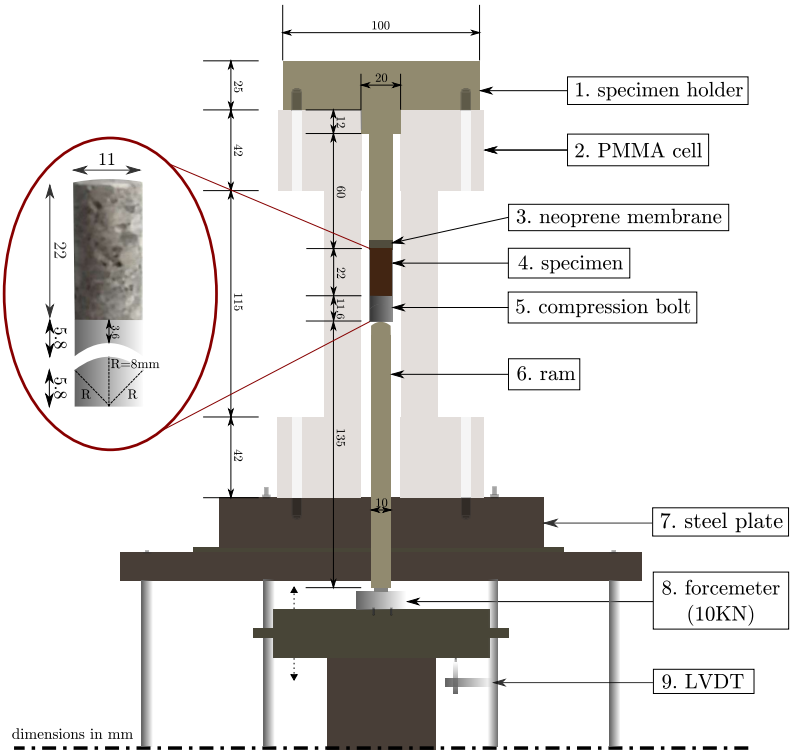

(a)

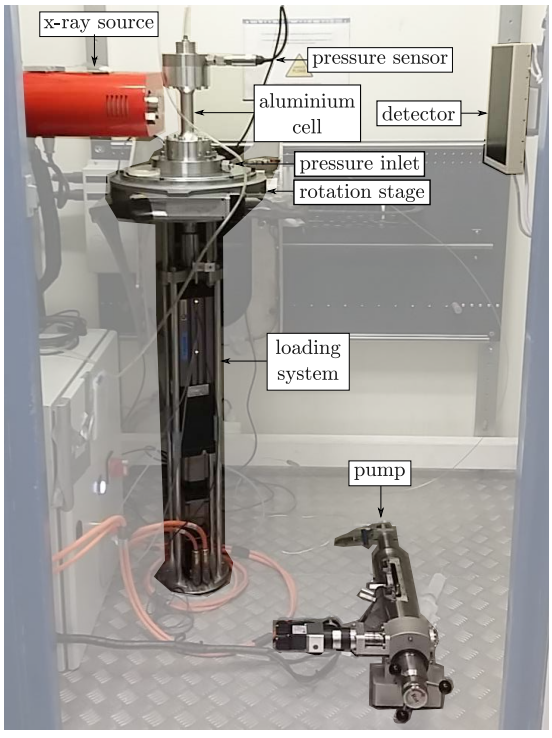

(b)

Figure 1: Experimental set-up for *in-situ* tests: (a) Sketch of the load frame for uniaxial compression tests, (b) Photo of the set-up for triaxial tests in the x-ray facility of Laboratoire 3SR. The designed high pressure aluminium loading cell is shown in place (mounted on the rotation stage), along with the pump used for the application of the confining pressure

LVDT (label No. 9 in Fig. 1a) is used to measure the vertical displacement of the loading

head.

Due to the use of x-rays, to balance the load applied to the specimens, the entire load frame is built upon a loading cell bolted into a steel plate (label No. 7 in Fig. 1a) which is, in turn, bolted into the rotation table. The loading cell needs to be made from a material which does not block the x-rays, but also be stiff enough to carry the return force. Considering that the strength of concrete increases with the confining pressure, there is a need to reach much higher axial force levels in case of triaxial tests, while sustaining the desired cell pressure. Therefore, the loading cell used for the triaxial tests differs from the one used for the uniaxial tests. The description of the set-up used for each type of test is given below.

2.2.1. Uniaxial compression

Concerning the uniaxial tests, a low x-ray absorption plexiglas cell (PMMA) is used. This cell, originally designed for triaxial testing of rocks up to 7 MPa confining pressure [Fonseca et al. (2013); Alikarami et al.], is shown as a sketch in Fig. 1a (label No. 2). It has a cylindrical hole of 20 mm diameter all the way through and a reduced wall thickness of 15 mm in the central part, where the cone x-ray beam is going to pass through. This particular "I" shape of the cell provides the necessary rigidity, but also allows the entire set-up to be translated very close to the x-ray source, allowing smaller pixel sizes to be reached thanks to geometric magnification. The fact that the cell is made of a transparent plastic allows visual monitoring during the test.

In order to erase any perpendicularity and parallelism defects of the specimen faces, a two-part specimen alignment mechanism (compression bolt, label No. 5) is designed. This compression bolt, made of steel, allows the specimen to rotate around the loading axis, eliminating any bending moment. As shown in Fig. 1a, it is placed in-between the bottom surface of the specimen (label No. 4) and the ram (label No. 6). In order to hold both the specimen and the compression bolt in place, a neoprene membrane (label No. 3) is used with an internal diameter of 10 mm and thickness of 0.5 mm. This membrane is stretched around the specimen, the pivot mechanism and a top platen (specimen holder, label No. 1) so as to cover at least few millimeters. The top platen is, in turn, bolted into the cell. Note that due to the plexiglas cell used, the loading system is not very stiff, resulting in a high elastic deformation of the whole loading frame. It is thus not possible to capture the post-peak phase of a uniaxial compression test on the micro-concrete specimens.

2.2.2. Triaxial compression

Due to the forcemeter used (10 kN maximum load capacity) and the selected specimen size, the maximum axial stress that can be applied on the sample is limited to about 100 MPa. For this level of axial stress, considering previous results on triaxial compression tests on similar concrete composition [Gabet et al. (2008); Vu et al. (2009); Poinard et al. (2012)], concrete samples can reach to failure for a confining pressure below 15 MPa. This maximum confining pressure (*i.e.*, 15 MPa), as well as the maximum axial load (10 kN), are then used as references to design a new confining cell. In addition to a strength criterion, a trade-off has also to be found between the stiffness and strength of the cell, allowing control of the post-peak response (which favours a thick cell) and its x-ray absorption (which favours a thin cell). Balancing these requirements results in the development of an I-shaped, high pressure 7075 T6 aluminium alloy cell, shown in Fig. 1b. Note that the technical drawings of this cell are presented in Appendix A.

Its shape and dimensions are similar to the plexiglas cell (used for simple compression), thus, fitting with the other pieces of equipment, but this time, with an external diameter

of 30 mm and a reduced wall thickness of 5 mm. The aluminium cell is bolted into the circular steel plate (label No.7 in Fig. 1a), which not only balances the forces carried from the cell, but also seals the bottom of the cell with an O-ring. The pivot mechanism and top platen are the same as the ones used for the uniaxial tests. However, unlike the plexiglas cell, a visual monitoring of the test is no longer possible.

An additional difference for triaxial test is the requirement of a filling system of confining fluid of the loading cell. The circular bottom steel plate has a tap on the outside (shown in Fig. 1b) that allows both the cell to be filled with water (*i.e.*, the confining fluid) and the confining pressure to be applied. A Sanchez VPSSH $6-700$ pump is used (shown in Fig. 1b) to allow a fine control of the confining pressure to the pressure value set. A neoprene membrane is used, again, to hold both the specimen and the compression bolt in place, as well as to ensure a watertight seal while the confining pressure is applied. This time, a triple layer of membrane is used to avoid any piercing due to punching of the membrane through the macro-pores that may be found on the specimen's surface. The top platen (or specimen holder), makes a seal with the top part of the cell and has a tap on the outside (shown in Fig. 1b). It is linked to a pressure sensor which is used to monitor the pressure level inside the cell during the test.

2.3. Test procedure, scanning parameters and test program

Once the set-up is ready, with the specimen mounted in the loading cell and positioned at the desired distance from the source (kept fixed during the whole test), the *in-situ* experiment can be conducted. Note that the number of scans and the loading steps are adapted for each test. This is justified by the fact that the loading is interrupted at different points attempting to catch significant changes in the macroscopic response. The choice of the loading steps is guided so as to have at least: one scan in the initial configuration (called reference scan), one in the elastic regime, several at intermediate load values before the peak and one last scan after failure. Since the exact strengths of the specimens are not known *a priori*, the loading steps are chosen approximately by combining information coming from the concrete composition and several preliminary mechanical tests performed in this work outside the x-ray scanner.

Concerning the uniaxial tests, the first tomographic scan is performed prior to any load application. In case of triaxial tests, after the loading cell is installed, it is filled from the top with tap water at room temperature with a syringe. The confining pressure is then applied with the Sanchez pump (see Fig. 1b) and once the desired pressure level is reached, the first tomographic scan is performed under isotropic compression. Due to the high pressure aluminium cell used for the triaxial tests, the probability of attenuating the x-rays passing through is higher. Therefore, different scanning parameters for each type of test are selected, which are summarised in Table 1. Note that both current and voltage are principal electrical quantities that can be adjusted in the tomograph used. By increasing the voltage, the speed of the accelerated electrons changes and, in turn, so does the x-ray photon energies. By adjusting the current, the amount of the accelerated electrons changes, *i.e.*, the flux of the beam changes.

In all experiments, when the first scan is completed, a compressive axial load is applied by moving the ram upwards with a constant displacement rate until the second loading step is reached. At this stage, the displacement is stopped and a second tomographic scan is performed. After this scan is finished, the specimen is loaded again, with the same displacement rate, until the next load step is reached. This sequence is repeated until the last scan, the one after the failure of the material, is conducted.

Table 1: Scanning parameters for uniaxial (PMMA cell) and triaxial (aluminium cell) tests

Parameters	Uniaxial	Triaxial
Source voltage [kV]	125	135
Source current [μA]	80	100
Source spot size	small	medium
Voxel size [μm]	13	13
Projections between 0° and 360°	1120	1120
Radiographs per °	6	7
Scan duration	1h50'	2h20'

In total, 6 *in-situ* experiments are conducted:

- 3 uniaxial compression tests (C-01, C-02 and C-03) and
- 3 triaxial compression tests at 5 MPa (TX5-01), 10 MPa (TX10-01) and 15 MPa (TX15-01) confining pressures.

Table 2 gives the main characteristics of the *in-situ* tests performed during the experimental campaign.

Table 2: Main characteristics of the *in-situ* tests: test name, confining pressure and number of scans performed

Test name	p [MPa]	# scans
C-01	0	5
C-02	0	8
C-03	0	6
TX5-01	5	5
TX10-01	10	6
TX15-01	15	6

The same loading-unloading paths are followed for the three uniaxial tests, with a first loading up to 2000 N, an unloading down to 200 N and a second loading until failure. Apart from the reference and the post-peak scans, in all of the tests, a scan at 2000 N is performed, during the first loading cycle and one at 2500 N, during the second loading cycle. The loading steps of 200 N, 2000 N and 2500 N correspond to a stress level respectively of about 2.1 MPa, 21 MPa (60% of the expected failure stress) and 26 MPa (70% of the expected failure stress).

Concerning the triaxial tests, in addition to the reference and the post-peak scans, a third scan is conducted at a relatively low force value. The objective of such a scan being to have a measurement in the elastic regime. It should be noted that for the *in-situ* test at the highest confining pressure (15 MPa), the limit of the force meter capacity (10 kN) was reached and as a result the loading had to be interrupted. However, the macroscopic response (discussed in Section 3.1 and shown in Fig. 9a) suggests that failure has already occurred. It is one of the cases where the measured kinematic fields are expected to shed some light on the failure mechanisms that occurred during the experiment.

2.4. Image analysis

2.4.1. Phase identification

The main advantage of performing an *in-situ* test is that, in addition to obtaining the macroscopic responses of the material, a set of 3D images is acquired at different loading

stages. Here, for each x-ray scan, a reconstructed 3D image is obtained by assembling the 2D radiographs using a filtered back projection algorithm, which is available in XAct software and provided by RX-Solutions (Annecy, France). This image represents a 3D field of x-ray attenuation coefficients inside the micro-concrete specimen, which is given as a greyscale scalar function.

Fig. 2 shows the mid-height horizontal slice extracted from the reference scan of the TX10-01 test (after the application of the confinement), along with the greylevel histogram of the 3D image. The shining point visible in the greyscale slice is a sign of the heterogeneity inside aggregates coming from different minerals. These minerals are much denser, attenuating many more x-rays and thus appearing with quite higher greyvalues in the reconstructed image. It can be seen that while the three phases of concrete's mesostructure are easily distinguishable by eye, their separation based on their greylevels is not trivial. Macro-pores appear in black (low x-ray attenuation) and are easy to separate, while coarse aggregates and mortar matrix (mix of finer aggregates and sand) share the same shades of grey (higher x-ray attenuation). The segmentation of each phase in this greyscale image is, thus, a first essential step.

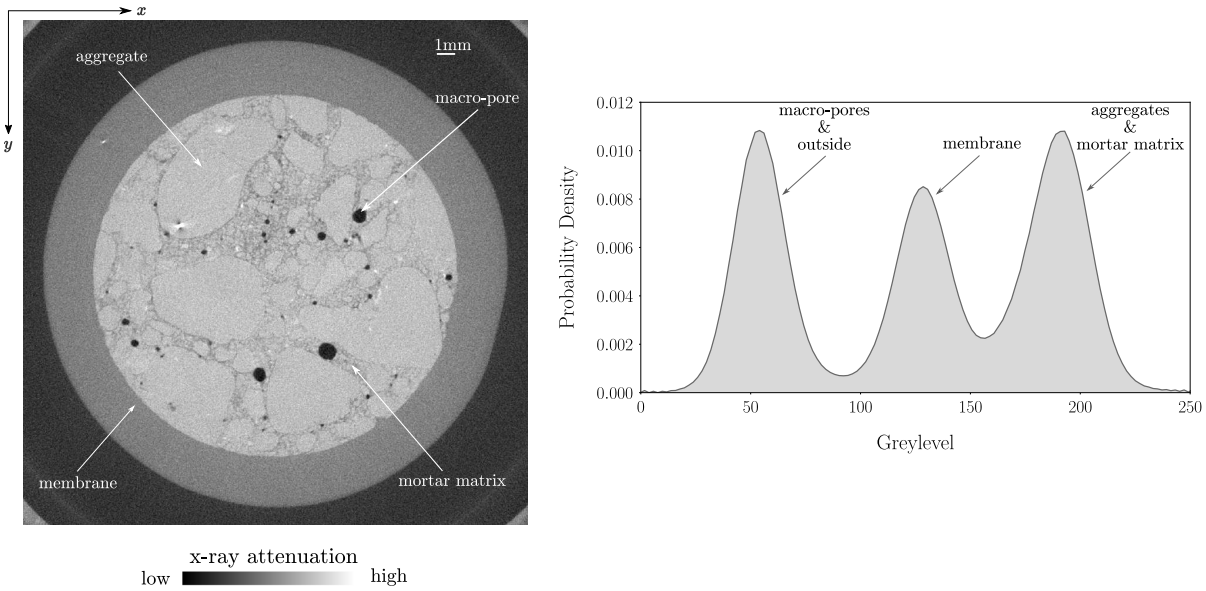

Figure 2: Mid-height horizontal slice and greylevel histogram of the reconstructed 3D volume of the TX10-01 test

This is achieved by applying the segmentation procedure proposed by Stamati et al. (2018). The principal technical challenge of separating the solid phase into aggregates and mortar matrix is addressed by calculating the variance map of the greyscale image (related to the homogeneity of the material), instead of relying on the absolute grey values (related to the density of the material). This segmentation technique exploits the fact that the local contrast, and thus, the texture inside aggregates and mortar matrix differs significantly, with the former identified thanks to their lower variance.

Once the three phases are separated, a quantitative characterisation of the morphology is possible. The computed macro-porosity of the tested samples ranges between 1.7 and 3.9%, while the percentage of aggregates ranges between 42.9 and 51.3%. Aggregates and macro-pores size distribution curves are shown in Fig. 3 for two representative tested samples. It should be reminded that the micro-concrete composition considered herein consists of aggregate sizes ranging between 0.5 and 4 mm, values that are in accordance

with the computed size distribution curves. Note that the discrepancy of the computed sizes between the tests is lower for aggregates compared to macro-pores, which is expected, since the latter are randomly created during the mixing of concrete.

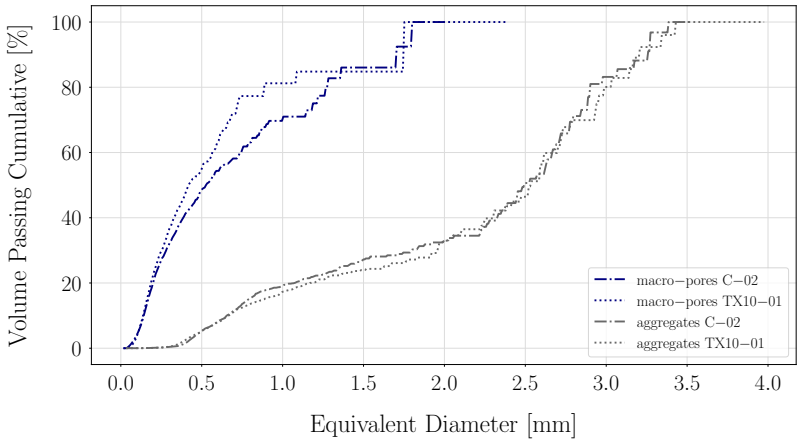

Figure 3: Aggregates and macro-pores size distribution curves for representative tested samples

2.4.2. Digital Volume Correlation (DVC)

The full-field measurement technique of Digital Volume Correlation (DVC) [Bay et al. (1999)] is employed to measure the 3D kinematic fields (displacement and strain fields) from the series of images coming from each test. The basic principle of DVC consists in finding a transformation that links two 3D images of the same sample acquired at different deformation increments. Herein, the open-source software `spam` [Stamati et al. (2020)] is used for the DVC analysis.

The correlation engine in `spam` aims to measure a linear and homogeneous deformation function, called hereafter $\mathbf{\Phi}$, such that the material point in the position $\boldsymbol{x}$ in the reference image corresponds to the same material point in the position $\boldsymbol{x}' = \mathbf{\Phi} \cdot \boldsymbol{x}$ in the deformed image. $\mathbf{\Phi}$ is expressed in homogeneous coordinates and represented by a 4×4 matrix that accounts for affine transformations: translation, rotation, normal and shear strain. The formulation of the correlation algorithm is based on a gradient-based iterative procedure, which minimises the difference between the reference and the deformed image, the latter being corrected by a trial deformation function (see Lucas et al. (1981); Tudisco et al. (2017) for more details). The convergence criterion is based on the norm of the deformation function increment between two successive iteration steps, which is set here as: $\|\delta\mathbf{\Phi}\| < 10^{-6}$. A maximum number of 300 iterations is also set as a limit to stop the iterative procedure in case that the convergence criterion is not satisfied.

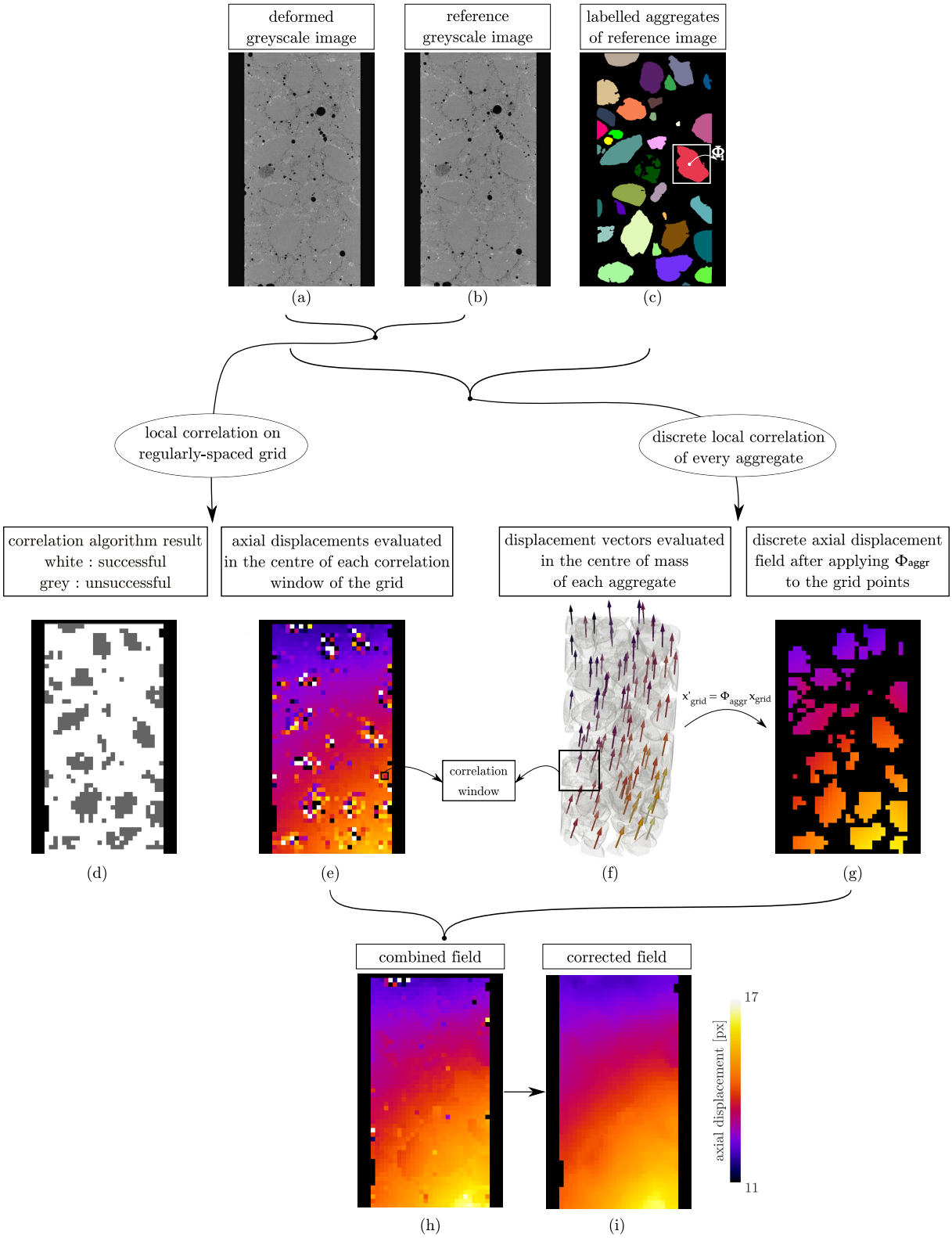

Figure 4: Illustration of the combination of the grid and discrete local DVC techniques in a pair of images coming from the C-02 test

A "local" DVC approach is used. An illustrative example of the proposed procedure is shown in Fig. 4 for a pair of images coming from the C-02 test. A regular grid of points is created by subdividing the reference image into a set of independent cubic subvolumes (*i.e.*, correlation windows), which are sought in the deformed image. The spacing of the

grid points is set equal to the window size (*i.e.*, contiguous correlation windows), ensuring a statistical independence of the corresponding error (see Grédiac and Hild (2013) for more details). By applying the iterative procedure on each subvolume, a $\mathbf{\Phi}$ is computed in the centre of each window. This yields a set of independent measurements that can be seen as a field of deformation functions for the whole image. The displacement field can be then obtained by extracting the translation component of each $\mathbf{\Phi}$ (see the axial displacement field on Fig. 4e).

It is important to stress here that the performance of the correlation is strongly affected by the texture in the bulk of the material. This texture needs to have sufficient contrast to give a unique signature to each subvolume considered. In the present case, while a fine grid is required to capture small micro-structural changes at the meso-scale, too small subvolumes can lead to low variance correlation windows, when positioned in textureless aggregates. In other words, a highly spatially resolved correlation field is rather ill-fated inside the coarse aggregates of the specimens (see the result of the grid correlation on Fig. 4d).

To circumvent this problem, a "discrete" correlation is performed aggregate-by-aggregate, as proposed by Hall et al. (2010) and Andò et al. (2012). Starting from the binary image of the segmented aggregates, a "labelled" image (see Fig. 4c) is created by assigning to all voxels belonging to each particle a unique positive integer (*i.e.*, label number). The greyvalues corresponding to each aggregate are then masked and arbitrarily shaped correlation windows are extracted, centered in the centre of mass of each particle. These subvolumes define the smallest box that each aggregate fits inside, the so-called "bounding box" (see rectangle of Fig. 4c), and are matched with the deformed image based on the iterative procedure mentioned previously. A deformation function is thus measured at the centre of mass of each aggregate, yielding a second field of discrete measurements for the whole image (see Fig. 4f).

The local grid measurements whose correlation procedure did not converge due to being inside an aggregate (see Fig. 4d) can now be replaced by applying the aggregate's measured deformation function to the grid point. Note that this operation results in a nonuniform displacement field inside each aggregate (see Fig. 4g). A deformation function that encodes a rigid-body rotation around the aggregate's centre of mass will add an angular displacement to the grid points belonging to this aggregate.

The combined displacement field (see Fig. 4h) is improved compared to the original one coming from a regular grid correlation (see Fig. 4e). However, this combined field contains a few points with extreme displacement values, either belonging to an aggregate that did not correlate successfully (see top left of the field) or to some points in the grid corresponding to the other two phases (mortar matrix or macro-pores) that also failed to correlate. To overcome this, the displacements of these grid points are replaced by the mean weighted (based on the distance) displacement values of the 12 closest successfully correlated points. Before proceeding into the strains calculation, this resultant displacement field is smoothed by applying a 3D median filter of a 1 voxel radius[3]. The result of this correction operation can be seen in Fig. 4i.

Strains are obtained by performing a linear mapping of $2 \times 2 \times 2$ neighbouring displacement measurements in order to compute the transformation gradient tensor $\boldsymbol{F}$ using standard finite element Q8 shape functions. Following the finite large-strain framework,

[3]The choice of the minimum possible (*i.e.*, one) voxel radius reduces the risk of oversmoothing the field and thus losing mechanical information.

for each Q8 element, a polar decomposition of $\boldsymbol{F} = \boldsymbol{R} \cdot \boldsymbol{U}$ yields the right stretch tensor $\boldsymbol{U}$ and the rotation tensor $\boldsymbol{R}$. The volumetric strain is given by the Jacobian determinant of $\boldsymbol{F}$: $\varepsilon_{\mathrm{V}} = det(\boldsymbol{F}) - 1$. Based on a multiplicative decomposition of $\boldsymbol{U}$ into an isotropic and deviatoric part, the deviatoric strain is given by the norm of the deviatoric tensor: $\varepsilon_{\mathrm{D}} = ||\boldsymbol{U}^{\mathrm{dev}} - \boldsymbol{I}||; \quad \boldsymbol{U}^{\mathrm{dev}} = det(\boldsymbol{F})^{\frac{-1}{3}}\boldsymbol{U}$.

2.4.3. DVC measurement uncertainties

The level of uncertainty in the DVC procedure is estimated through a so-called "repeated" scan. Two scans of the same micro-concrete sample are performed with some rigid-body motion between the two acquisitions, but without any mechanical loading. Two different "repeated" scans are conducted; one for the uniaxial and one for the triaxial tests, using the corresponding loading cells and scanning parameters discussed in Section 2.3.

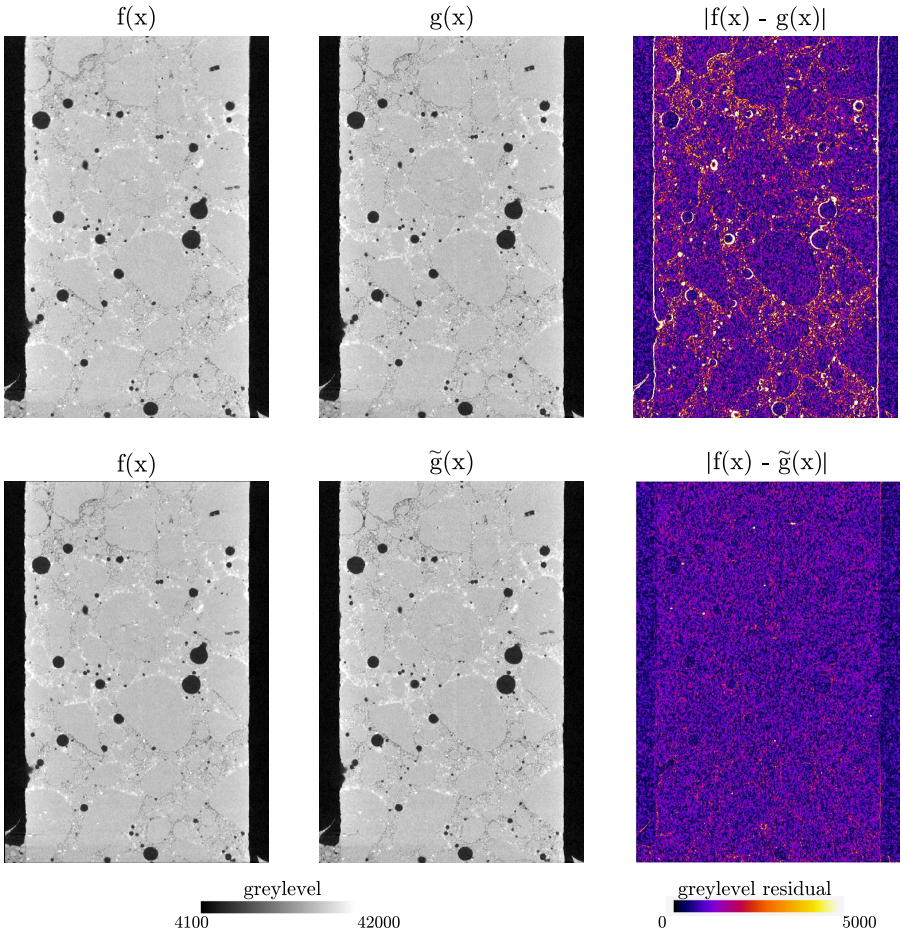

Figure 5: Registration of the "repeated" scan for the uniaxial (PMMA cell) tests. (Top): central vertical slices of the two scans along with their initial difference, (Bottom): central vertical slices of the reference image (same as above), the registered second image and their difference after their registration

Fig.5 depicts the central vertical slices of the pair of images coming from the repeated scan for the uniaxial tests. Their initial absolute difference (top right) is calculated by voxelwise subtracting the greyvalues in the two images and keeping the absolute value of their difference. This difference image demonstrates that even though no mechanical loading has occurred, there is some rigid-body motion between the two configurations, as

well as accumulated noise throughout the acquisition and the reconstruction procedure. These two images are "registered" (*i.e.*, aligned) by computing a single and homogeneous deformation function $\mathbf{\Phi}$ which maps all of the reference image to the second one. The new difference image $|f(\boldsymbol{x}) - \widetilde{g}(\boldsymbol{x})|$, where $\widetilde{g}(\boldsymbol{x})$ corresponds to the image of the second scan after the application of the measured $\mathbf{\Phi}$, is shown on the bottom right of Fig.5. The underlying meso-structure is no more visible, indicating that the two images are well aligned.

After the subtraction of the measured rigid-body motion, the remaining non-zero intensity values in the difference image are an indicator of the measurement uncertainty, which is attributed to the inherent noise of the data and is intrinsic to the DVC procedure. This measurement uncertainty is quantified through a series of local DVC computations for a large range of contiguous cubic correlation window sizes. For this parametrical analysis, the correlation windows that fall completely inside large aggregates (and thus fail to correlate) are not considered. As explained above, before proceeding into the strains calculation, the displacement fields are corrected and filtered.

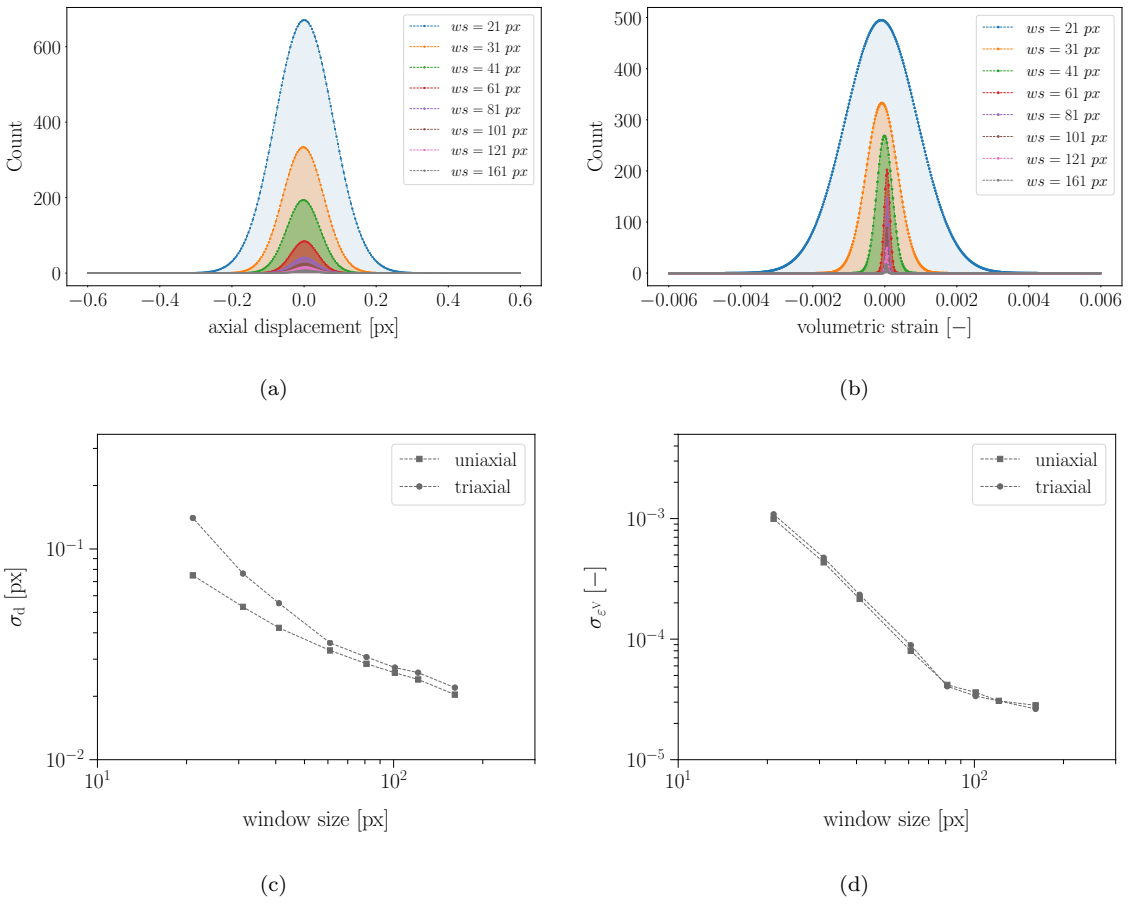

Figure 6: Estimation of DVC measurement uncertainties for uniaxial (PMAA cell) and triaxial (aluminium cell) tests. (Top): Histograms of measured axial displacement (a) and volumetric strain (b) for a range of window sizes for the uniaxial tests. (Bottom): Evolution of the standard deviation of the displacement magnitude (c) and the volumetric strain (d) as a function of the correlation window size for both types of tests

The histograms of the axial displacement and volumetric strain for a range of correlation window sizes are presented on the top row of Fig. 6 for the uniaxial test (PMMA cell). They both fit a Gaussian distribution indicating that the measurements correspond

to random noise. The evolution of the standard deviation of the displacement magnitude and the volumetric strain as a function of the correlation window size for both types of tests (PMMA and aluminium cell) is shown on the bottom row of Fig. 6.

A well-known trend is observed [Hild and Roux (2012); Grédiac and Hild (2013)], where there is a clear trade-off between the spatial resolution of the measurement and the level of the measurement uncertainty. On one hand, a precise description of a complex heterogeneous kinematic field requires many measurement points (small window sizes). On the other hand, a too small window size leads to higher uncertainties which can dominate the signal. Considered as the best compromise, the selected window size is set to 31 voxels (*i.e.*, 0.4 mm), which is 1/10 of the largest aggregate size. It means that any measured displacement smaller than 0.05 px for the uniaxial tests and 0.08 px for the triaxial tests falls below the uncertainty level. The choice of this correlation window size excludes the coarser aggregates, which as explained before are independently correlated in a much larger zone of interest, defined by their bounding box (see Fig. 4c). Note that based on the displacement uncertainty analysis, an estimation of the global error on the Young's modulus measurement (*i.e.*, ΔE [GPa]) can be also derived, as described in Appendix B.

3. Results

3.1. Macroscopic measurements

The macroscopic responses are first discussed. The stress-strain curves measured during the tests are presented after subtracting the displacement corresponding to the loading system. To evaluate the latter, for each type of test, the stiffness of the system, assumed linear elastic, is measured with a calibrated steel sample. It is recalled here that for the uniaxial tests the loading system is not stiff enough to capture the post-peak, mainly because of the plexiglas cell used.

As an illustration of a uniaxial compression test, the macroscopic response of the C-02 test is shown in Fig. 7. The loading steps for which the tomographic scans are carried out are indicated, as well as the reconstructed 3D images of the specimen. The response is typical of a concrete specimen being uniaxially compressed, with a compressive strength of 38 MPa and a Young's modulus of 29 GPa. Due to the plexiglas cell used, the elastic energy stored in the loading system is larger than the energy the sample is able to dissipate. Therefore, even though quasi-brittle, the post-peak response is not captured. A contact effect (revealed by a non-linear behaviour) can be seen at the beginning of the loading between the two-part compressive bolt (see Fig. 1a) and the specimen whose faces are not perfectly plane. However, the failure pattern observed in the post-peak 3D image does not reveal any contact cone due to friction between the sample faces and the loading caps. It is worth mentioning that even if a complex failure pattern is observed in the last scan, no obvious micro-structural change is visible in the images before the peak.

As an illustration of a triaxial compression test, the deviatoric part of the TX10-01 test is shown in Fig. 8, as well as the reconstructed 3D images at each loading step. The measured Young's modulus is 25.5 GPa and the peak deviatoric stress is 98 MPa. Unlike the uniaxial tests, due to the hydrostatic loading, a linear elastic response is observed from the very beginning of the deviatoric loading. It is followed by a loss of stiffness due to micro-cracking. The deviatoric stress is increased until the strength of the material is reached, whereafter strain softening occurs. Similarly to the C-02 test, no obvious micro-structural change is visible in the 3D images before the peak.

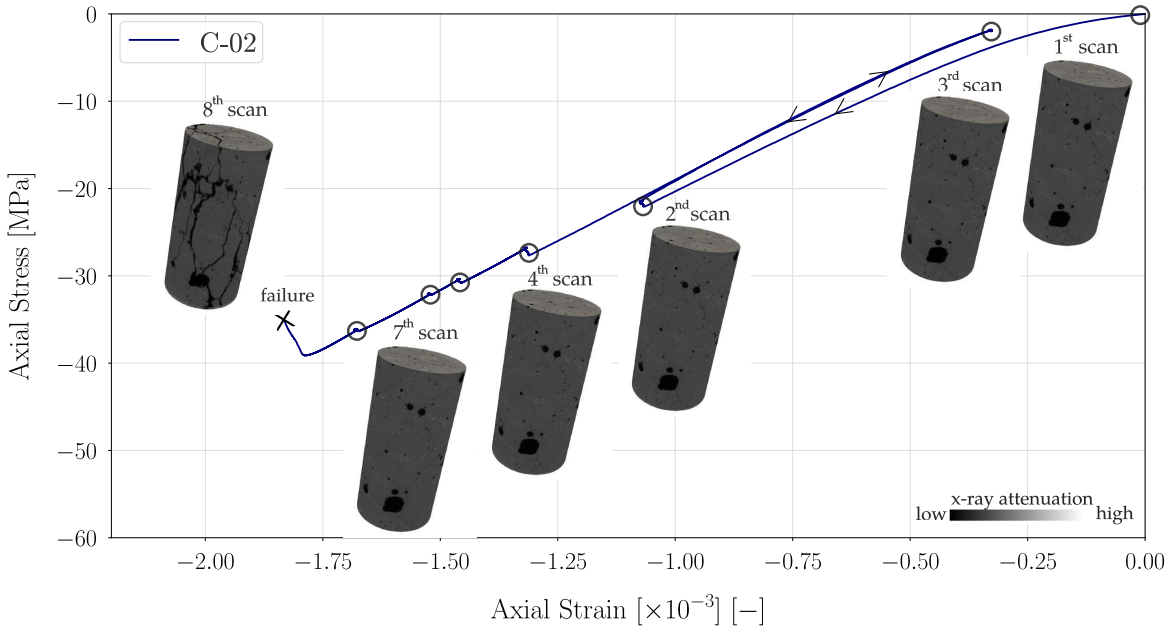

Figure 7: Macroscopic stress-strain curve for the C-02 uniaxial compression test performed *in-situ* in the x-ray scanner

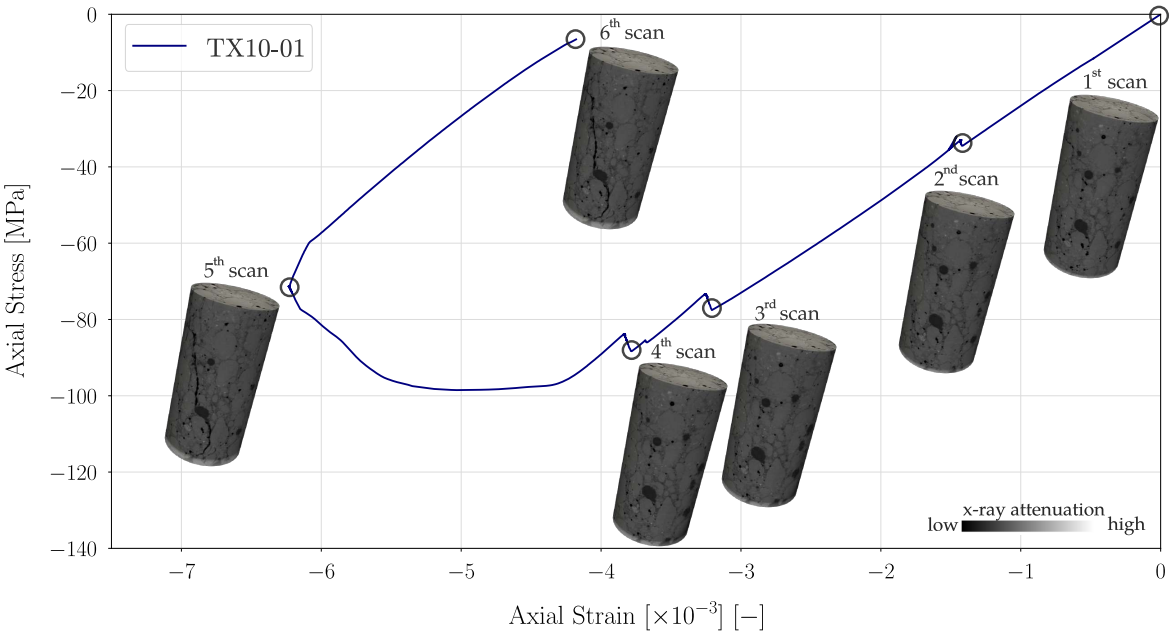

Figure 8: Deviatoric part of the macroscopic stress-strain curve for the triaxial compression test under 10 MPa confinement (TX10-01) performed *in-situ* in the x-ray scanner

The macroscopic responses for all the *in-situ* mechanical tests are gathered and presented in Fig. 9a. Note that for the uniaxial tests only the part starting from the second loading cycle is shown, while for the triaxial tests only the deviatoric part of the tests is shown. The mechanical responses of the tested samples seem to be representative of the ordinary concrete from which the micro-concrete composition is derived, despite the fact that the specimens' size is not very large compared to the largest aggregates. As the

confinement increases, the samples' strength is increasing, as well as the level of stress relaxation during scanning. Another trend that is observed is the passage from brittle to ductile behaviour, corresponding to the transition between fracture mode I and fracture mode II [Reynouard et al. (2010)].

Fig. 9b depicts the loading paths of all the tests in the stress space (meridian plane) using the first two stress invariants: the deviatoric stress, *i.e.*, $q = |\sigma_1 - \sigma_3|$, as a function of the mean stress, *i.e.*, $\sigma_m = |(\sigma_1 + 2 \times \sigma_3)/3|$. By plotting the evolution of the maximum deviatoric stress versus the maximum mean stress, for all the tests, a stress limit state curve (*i.e.*, failure surface) is obtained. This limit state curve is non-linear and well described by a three parameter power law, which was proposed by Malecot et al. (2019) and written as:

$$q_{max} = q_1 \left(\frac{\sigma_m - \frac{f_{ck}}{3}}{q_1} + \left(\frac{f_{ck}}{q_1} \right)^{\frac{1}{\alpha}} \right)^{\alpha} \tag{1}$$

where f_{ck} is the unconfined compressive strength, while the two parameters q_1 and α depend on the behaviour of the fully compacted concrete, called granular stacking (aggregates and cement paste without any strength or residual porosity) and vary according to the aggregate type and size (see Vu et al. (2011) for more details). The value of f_{ck} is directly deduced from the uniaxial compressive tests (f_{ck} =38 MPa). The values of q_1 and α, given in Table 3), are initially taken from Malecot et al. (2019) and adjusted to fit the presented data. The predicted q_{max} based on the above criterion is plotted for a range of mean stresses and a very good fit with the experimental data is observed. Even though only a limited number of tests is examined here, this power law could be used to predict the failure criterion of concrete in the (q_{max}, σ_m) plane.

Table 3: Set of fitting parameters for the power law criterion given in Eq. 1 and shown in Fig. 9b

Parameter	Symbol	Value
Unconfined compressive strength	f_{ck}	38 MPa
Slope of the criterion on a logarithmic scale	α	0.77
Critical shear stress of dry concrete	q_1	1280 MPa

3.2. Fracturing process and failure patterns

After the investigation of the macroscopic responses of the samples for different loading paths, the damage initiation and evolution until failure is studied. As presented in Section 2.4, the kinematic fields are obtained through a combination of a local DVC computation on a fine regularly-spaced grid (contiguous correlation windows with a point spacing of 31 voxels, *i.e.*, 0.4 mm) with a "discrete" correlation of the coarser aggregates. The measured fields are presented as total fields and not as incremental. This means that the first scan of each test is always considered as the "reference" configuration and is mapped into the subsequent scans captured throughout the experiment. Note that for the uniaxial tests, since the response of the material is too brittle, no correlation between the reference and the post-peak scan is performed.

Fig. 10 gathers the DVC displacement fields at different loading stages for compressive tests from 0 to 15 MPa confinement. Before the peak, relative displacement magnitudes of about 10 pixels (*i.e.*, 130 µm) are measured, with rigid-body translations of about 15 pixels (*i.e.*, 300 µm). For the first loading step (ranging between 40 to 60% of the failure load)

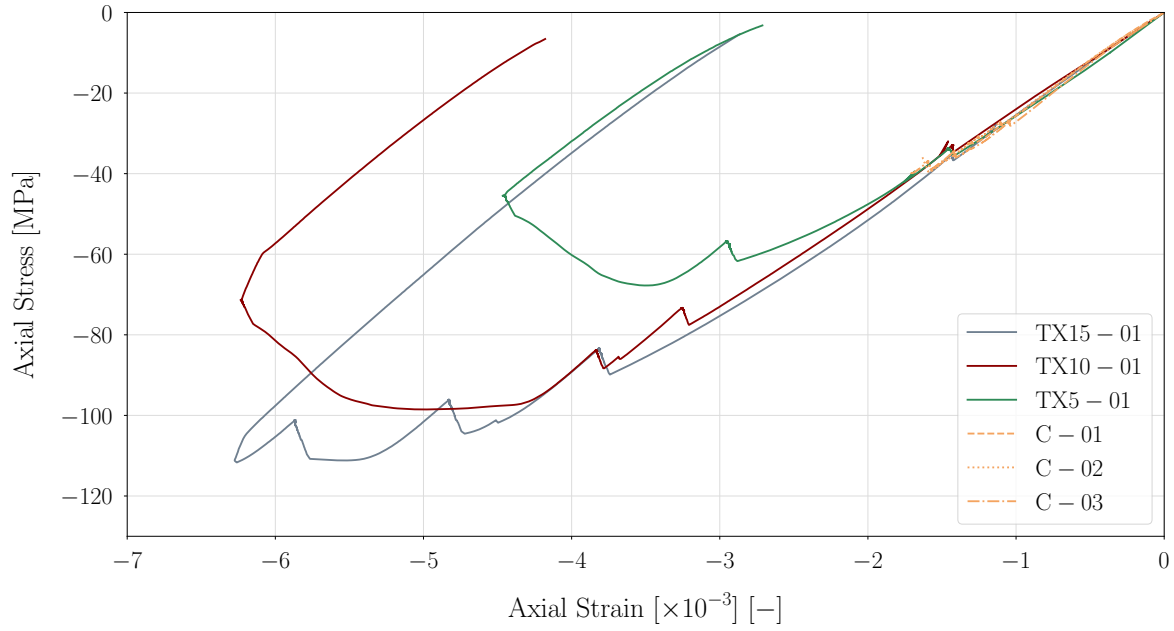

(a) Axial stress versus axial strain

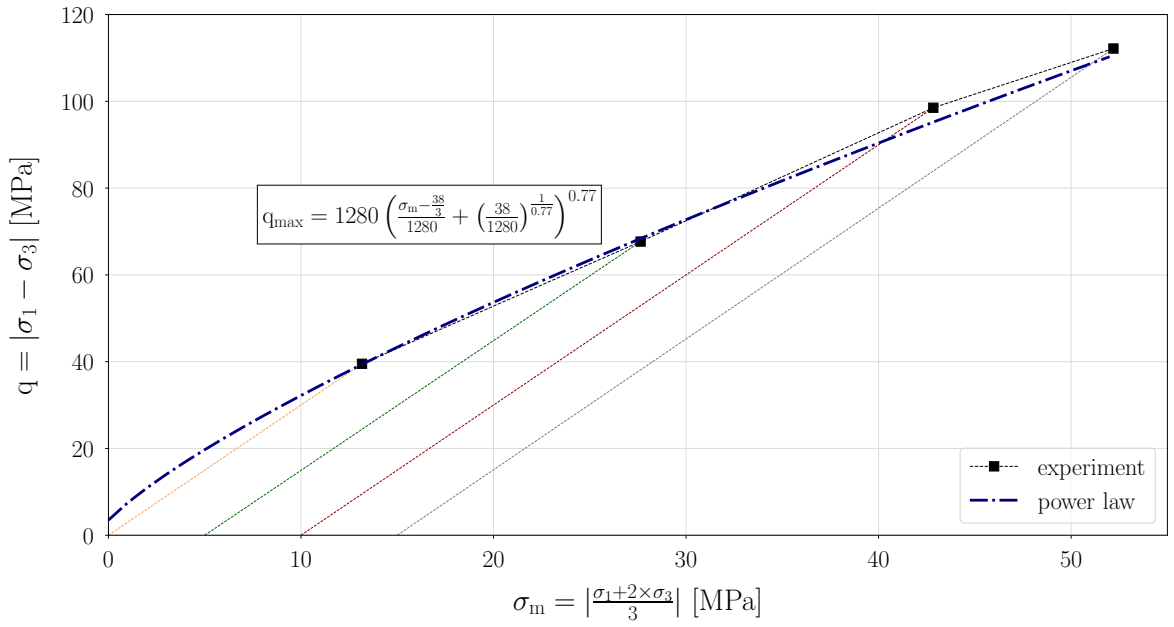

(b) Loading paths and failure surface (blue colour) in the meridian plane (deviatoric stress versus mean stress)

Figure 9: Macroscopic behaviour of *in-situ* tests

a smooth distribution of the displacements is observed for all tests. For the uniaxial test (Fig. 10a) and the triaxial test under the lowest confinement (Fig. 10b), the vectors point mostly upwards (although, slightly tilted on the top part for the TX5-01 test), indicating the direction of the applied compressive load. As the level of the confinement increases (Fig. 10c and Fig. 10d) the vectors are rather tilted on the side, with higher magnitudes at the bottom part (see length of the arrows), where the deviatoric load is applied. Table 4

presents the macroscopic Young's moduli and their corresponding errors[4] derived from the top and bottom axial displacements at these first loading stages. They range between 24.5 to 27 GPa, with a corresponding error of about ±3 GPa, which are in a good agreement with the values obtained directly from the stress-strain macroscopic curves.

Table 4: Young's moduli and corresponding errors measured through DVC

Test name	E [GPa]	ΔE [GPa]
C-02	27	±4
TX5-01	24.5	±2
TX10-01	25.5	±2
TX15-01	26.5	±2

As the loading increases, the displacement fields become more irregular. Inclined bands of displacement gradients across the specimen can be seen in C-02 test. They progressively become more pronounced, suggesting localised regions of strain, slightly inclined compared to the axial direction. For the triaxial tests, as the deviatoric load progresses, the magnitude of the displacement increases with displacement vectors clearly tilting compared to the axial direction. At the end of both TX5-01 and TX10-01 tests (after failure), the displacement fields consist of two discrete blocks, with an inclined zone of high displacement gradient in-between them, suggesting a shear failure along an inclined surface in the specimen. Unlike TX5-01 and TX10-01 tests, the evolution of the displacement field, as well as the final failure mode are very different for the test under the highest confinement (Fig. 10d). In this case, with an increase of the deviatoric loading, the orientation of the displacement vectors do not point in a parallel tilt, but rather a block, exhibiting a constant displacement magnitude, appears in the bottom of the specimen. Even though this test had to be interrupted, the displacement field in the last stage suggests that the failure happens in a roughly horizontal band located near the bottom part of the sample.

The displacement fields presented so far give an idea about the different failure modes. The investigation of the derived strain fields is then essential for following the localisation process in the specimens. This time, to facilitate the analysis of the deformation process, as well as to highlight the impact of the micro-structure, vertical slices of the strain fields are presented, overlaid with the largest aggregates identified from the segmentation of the reference scans. The slices extracted from the strain fields are chosen to include both the specimens' axis and prominent deformation patterns. The corresponding greyscale slices, extracted from the tomographic scans at each loading step, are also shown.

Fig. 11 presents the evolution of the volumetric strain field during the C-02 simple compression test. During the first stage (first column of Fig. 11), the specimen is mostly under uniform compression resulting in negative volumetric strain. Only in some few weak points displacement incompatibilities lead to stress concentrations, which in turn result to local expansion (*i.e.*, positive volumetric strain). Strain localisation is thus initially observed in the interfaces between aggregates and mortar matrix (weakest points due to material heterogeneities) scattered throughout the specimen. As the compressive load increases (second column of Fig. 11), some regions of transverse tensile strains around aggregates become more pronounced. Note that the width of these localised strain zones, directly related to the correlation window size which imposes the observation scale,

[4]The error is computed from the formula given in Appendix B.

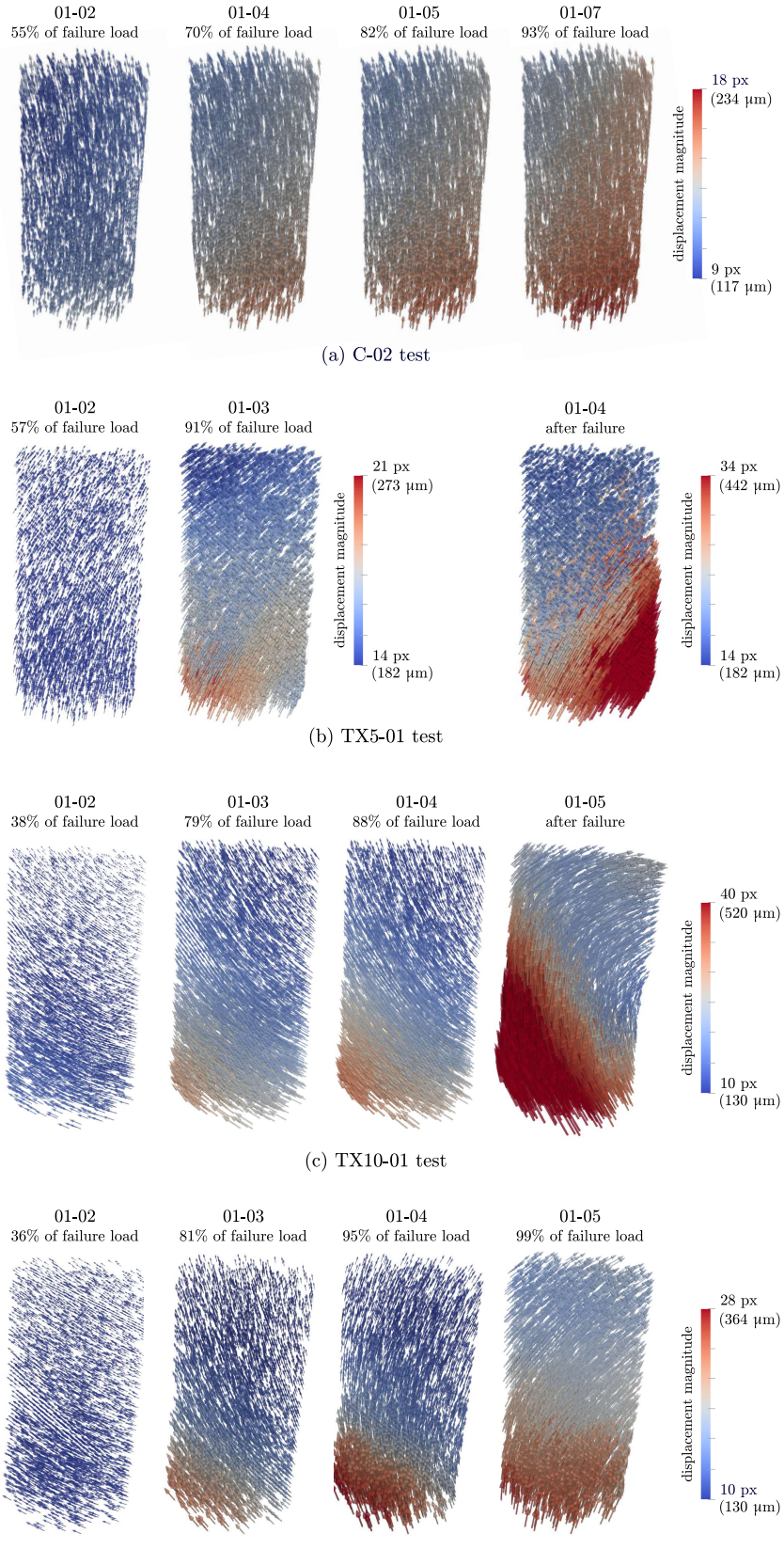

Figure 10: Evolution of DVC displacement fields at different loading stages for an increasing confining pressure (from 0 to 15 MPa)

measures about 0.6 mm. Close to the peak stress (93% of the failure stress) a highly heterogeneous strain field is observed (third column of Fig. 11). It is worth noting that, even though no damage is visible in the x-ray image at this loading step, the identified regions of localised strains coincide very well with the cracking network observed in the post-peak scan. The evolution of the volumetric strain field indicates that regions of localised strain around aggregates have propagated and bridged through the mortar matrix, leading to the development of the complex cracking network depicted on the post-peak scan. These identified regions of strain localisation are directly related to ITZs, which are well-known for being the weakest phase and thus responsible for concrete fracture. However, with the selected voxel size of 13 µm, a straightforward identification of the ITZs is not possible at this study.

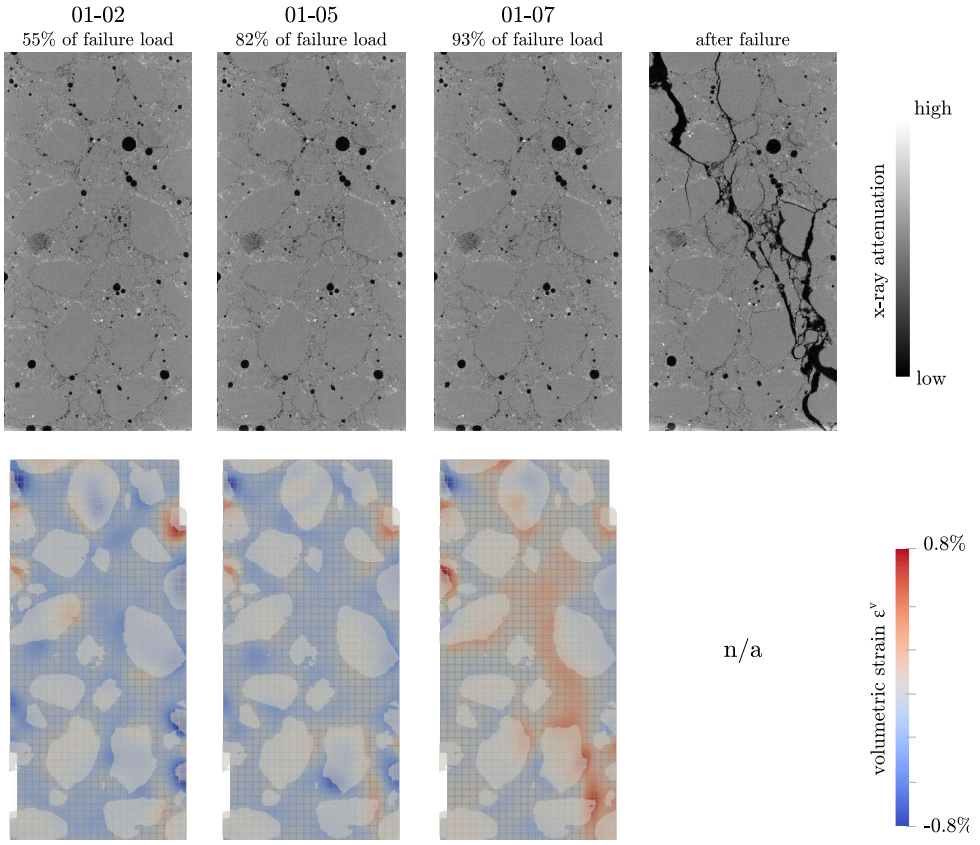

Figure 11: Evolution of volumetric strain field for C-02 test

Fig. 12 and Fig. 13 present slices of the evolving deviatoric strain fields of the TX5-01 and TX-10 tests, respectively. At the beginning of the loading, a rather homogeneous strain field is observed, with only few regions exhibiting higher deviatoric strains, mainly around aggregates. The strain localisation initiates well before the stress plateau as it can be observed in the second and third columns of Fig. 12 and Fig. 13, where regions of significant localised deviatoric strains can be seen. It is worth noting that the width of these regions is larger (about 1.5 mm) compared to the one of the uniaxial test (about 0.6 mm). These regions have the same orientation with the shear failure bands that are observed in the right column of Fig. 12 and Fig. 13. The inclination and location of the formed shear bands seem highly influenced by the presence of the coarse aggregates. Note that the amplitude of the deviatoric strain measured along these bands is not constant, even if one has to be careful about the physical meaning of the strain measured inside such a strong discontinuity.

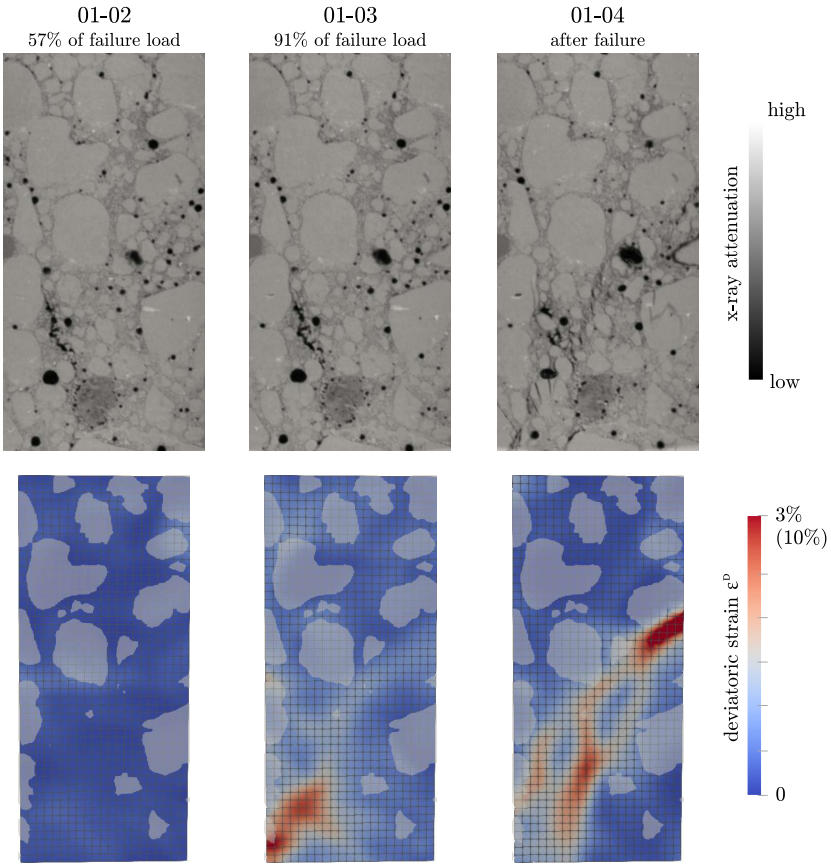

Figure 12: Evolution of deviatoric strain field for TX5-01 test

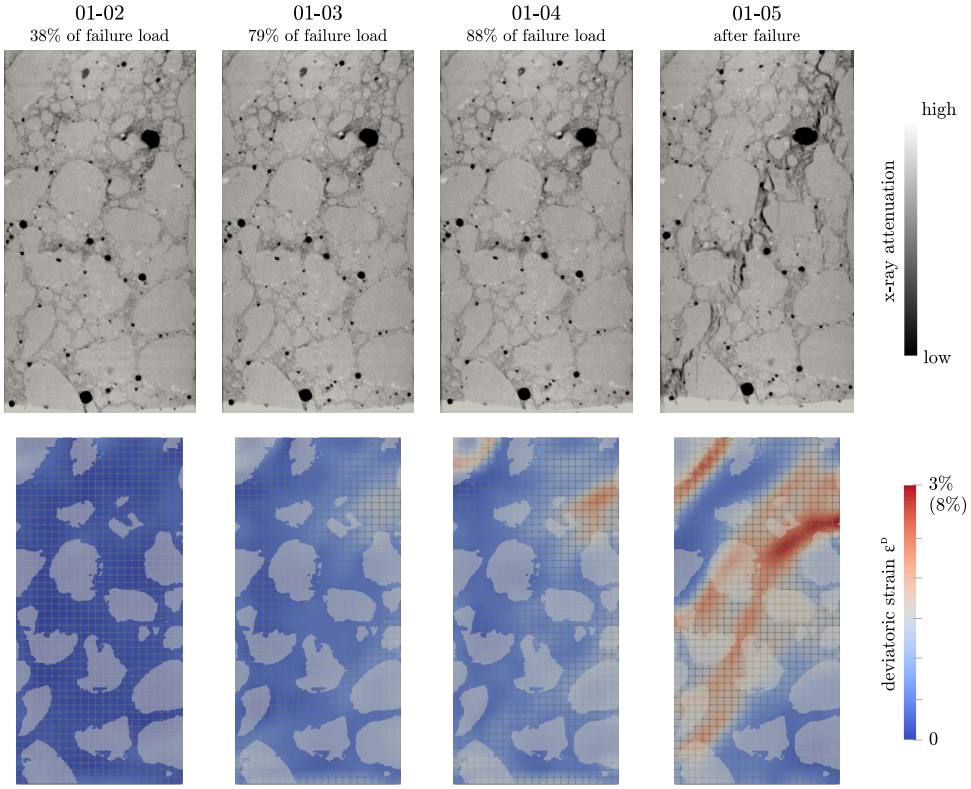

Figure 13: Evolution of deviatoric strain field for TX10-01 test

The evolution of both the deviatoric and the volumetric strain fields during the triaxial test under the highest confinement (TX15-01) is presented in Fig. 14. As previously, for the first loading step, both strain fields are rather uniform, while with the increase of the deviatoric loading, strain concentrations appear around aggregates, mainly at the bottom part of the specimen (second column of Fig. 14). Reaching closer to the plateau of the deviatoric stress, the strain localisation gets more pronounced with deviatoric strain accumulating within a shear band in the bottom part of the sample (third column of Fig. 14). The increase of the deviatoric strain is associated to a corresponding increase of the compaction, highlighted by the volumetric strain field (negative values). In the last loading step, the formation of a compactive shear band slightly inclined with respect to the principal stress direction is observed. It is worth mentioning the impact of the largest macro-pores in the progressive development of this compactive shear band.

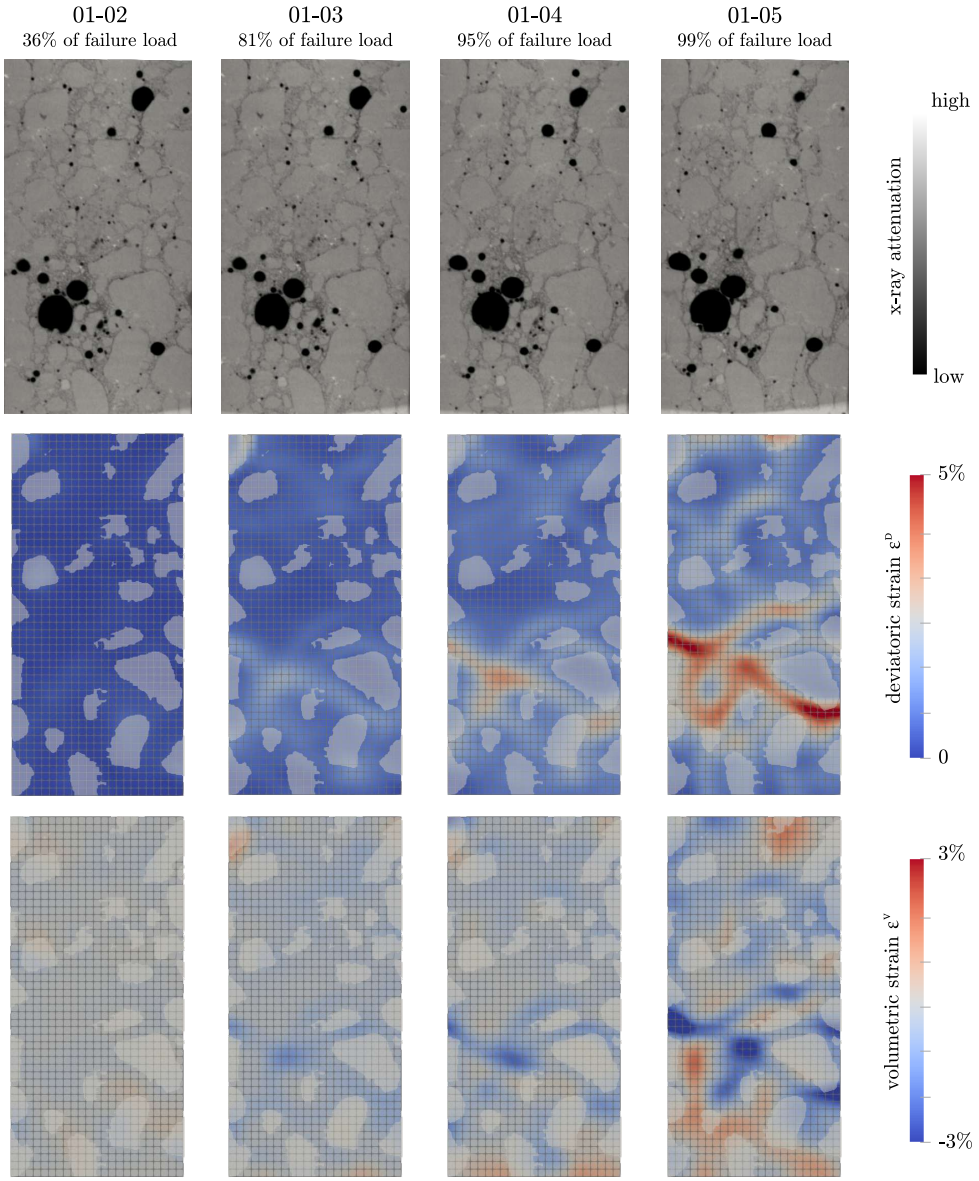

Figure 14: Evolution of deviatoric and volumetric strain fields for TX15-01 test

Fig. 15 gathers the 3D visualisations of the failure modes of the different samples at the end of the loading. The largest heterogeneities of the reference scans (macro-pores and coarse aggregates) obtained from the segmentation are presented together with the

cracking networks. A clarification should firstly be made on how these cracking networks are extracted. For the uniaxial tests, the macro-cracks are of some pixels width and thus easily visible in the post-peak images. This results in their direct identification by a thresholding operation based on their greyvalues. However, in the case of triaxial tests, cracks might be too narrow to be visible, with widths less than the voxel size (see right column of greyscale slices in Fig. 12 to 14). It is thus difficult to directly extract them from the post-peak scans.

A finer detection of the cracking network is achieved for each triaxial test thanks to the correlation residual fields between the reference and the post-peak scan. This field represents the difference (in greylevels) between the images in the reference and the post-peak configuration, after the former has been corrected by the measured deformation field. Correlation residual fields are valuable for revealing the noise contained in the 3D images (see Fig. 5), but also intrinsic errors to the kinematics assumed by the DVC procedure. Provided that the deformation function $\mathbf{\Phi}$ accounts only for linear transformations (see Section 2.4), high residual values are indicators of discontinuities on the measured displacement field, corresponding to cracks.

For the uniaxial test (Fig. 15a), the failure pattern consists in several macro-cracks branching around aggregates roughly parallel to the axial loading direction. Note that some cracks have propagated through some aggregates (see for example the fractured aggregates of Fig. 11). Complex network of cracks crossing the specimens diagonally, branching around the coarser aggregates and propagating through the macro-pores are observed for the triaxial tests at the lowest confining pressures (Fig. 15b and Fig. 15c). However, as already mentioned, the failure mode occurred for the test under the highest confinement (Fig. 15d) is quite different. Concentrations of high correlation residuals values appear as a horizontal band near the bottom part of the sample. Observing the internal meso-structure, this region corresponds to a relatively high concentration of porosity. It suggests that, unlike TX05-01 and TX10-01 tests, not the micro-cracking, but rather the collapsing of the porous structure of the material is most likely to be the principal local damage mode that leads to the macroscopic failure of the specimen.

As a last important remark, by observing the crack patterns at the end of each test, the failure occurs far from the boundaries of the samples. For instance, no contact cones at the edges of the samples are observed in simple compression, which is a rather common boundary effect problem. In addition, based on the presented DVC analysis, the initiation of failure occurred away from the borders. Although the specimens are admittedly small compared to the size of the largest heterogeneities, the above remarks lead to a conclusion that the influence of the boundary conditions is weak.

4. Discussion and conclusions

This work presented an experimental study of the deformation and damage process of concrete at the meso-scale. The mechanical response of small cylindrical micro-concrete samples (*i.e.*, 11 mm in diameter and 22 mm in height) of realistic composition (including cement, sand, aggregates and water) was studied under different loading paths. A suitable experimental set-up compatible with a typical laboratory x-ray scanner was developed, allowing the micro-concrete specimens to be scanned while they were subjected to uniaxial or triaxial compression at 5 MPa, 10 MPa or 15 MPa confining pressures, which to the knowledge of the authors is unique in the literature.

Despite their admittedly small size, the specimens were proven to be mechanically representative of the ordinary concrete from which the micro-concrete composition was

(a) (b) (c) (d)

Figure 15: Crack patterns (dark grey) at the end of the loading along with the segmented largest heterogeneities (macro-pores in black, coarse aggregates in light grey) of the reference scans; (a): C-02 test, (b) TX5-01 test, (c) TX10-01 test and (d) TX15-01 test

derived. The values of the measured Young's moduli and compressive strengths were close to those of ordinary concrete specimens. With an increasing level of confinement (from 0 to 15 MPa) the transition from brittle to ductile response was observed, as well as an increase of the strength of the material.

The first stages of the deformation and damage process at the scale of the largest aggregates and macro-pores were followed and quantified thanks to a DVC analysis of the set of 3D images coming from each *in-situ* test. To overcome the difficulty of correlating the textureless coarse aggregates, an original combination of a regularly-spaced local DVC technique (for the mortar matrix) with a discrete DVC technique (for the coarser aggregates) was proposed. Based on an uncertainty analysis, the spatial resolution of the grid points DVC measurements was set to 0.4 mm, which is 1/10 of the largest aggregate size.

A modification of the failure modes was observed with the increase of the level of confinement. In simple compression, a complex network of several macro-cracks branching around aggregates was developed, roughly parallel to the axial loading direction. Inclined shear bands, crossing roughly diagonally the specimens, were observed for the triaxial tests under 5 MPa and 10 MPa confining pressures. A compactive shear band, near the bottom of the specimen, almost perpendicular to the principal stress direction was observed for test under 15 MPa confinement. In all cases, the macro-cracks that lead to the samples failure were located thanks to DVC much before the peak stress, while the material is still cohesive. This observation highlights the strong impact of the underlying meso-structure on the local failure mechanisms. It was shown that the strain localisation mainly originated from the interfaces between aggregates and mortar matrix, with the shape and location of the largest aggregates and macro-pores essentially driving the propagation of the cracking network.

The experimental results presented in this article suggest that in order to accurately describe the complex fracturing process of concrete and obtain a fundamental understanding of its failure mechanisms, the actual material's meso-structure has to be taken into account. Such an experimental evidence encourages towards the development of numerical models which are based on a realistic representation of the meso-structure of the material. A numerical model, validated against experimental results like the ones presented herein,

can provide promising potentials for a global statistical analysis. Such an analysis should involve a large number of numerical samples subjected to a range of different loading paths. In the engineering context, such an approach could provide quantitative recommendations of the impact of each phase leading to the improvement of the strength and ductility of the material and, thus, to a better design of concrete mixtures.

Data Availability Statement

The reconstructed 3D images of selected tests and the corresponding DVC analysis are available on Zenodo: https://zenodo.org/record/3898495 with doi: 10.5281/zenodo.3898495.

CRediT author statement

All authors listed have made a substantial, direct and intellectual contribution to the work, and approved it for publication.

Declaration of interests

The authors declare that they have no known competing financial interests or personal relationships that could have appeared to influence the work reported in this paper.

References

Aggelis, D., Philippidis, T., 2004. Ultrasonic wave dispersion and attenuation in fresh mortar. NDT & E International 37, 617–631.

Alikarami, R., Andò, E., Gkiousas-Kapnisis, M., Torabi, A., Viggiani, G., . Strain localisation and grain breakage in sand under shearing at high mean stress: insights from in situ x-ray tomography. Acta Geotechnica .

Anay, R., Soltangharaei, V., Assi, L., DeVol, T., Ziehl, P., 2018. Identification of damage mechanisms in cement paste based on acoustic emission. Construction and Building Materials 164, 286–296.

Andò, E., Hall, S.A., Viggiani, G., Desrues, J., Bésuelle, P., 2012. Experimental micromechanics: grain-scale observation of sand deformation. Géotechnique Letters 2, 107–112.

ASTM, 2003. Standard test method for obtaining and testing drilled cores and sawed beams of concrete.

Balendran, R., Pang, H., Wen, H., 1998. Use of scanning electron microscopy in concrete studies. Structural Survey .

Basheer, L., Basheer, P., Long, A., 2005. Influence of coarse aggregate on the permeation, durability and the microstructure characteristics of ordinary portland cement concrete. Construction and Building Materials 19, 682–690.

Bay, B.K., Smith, T.S., Fyhrie, D.P., Saad, M., 1999. Digital volume correlation: three-dimensional strain mapping using x-ray tomography. Experimental mechanics 39, 217–226.

Brisard, S., Serdar, M., Monteiro, P.J., 2020. Multiscale x-ray tomography of cementitious materials: A review. Cement and Concrete Research 128, 105824. URL: http://www.sciencedirect.com/science/article/pii/S0008884619301887, doi:https://doi.org/10.1016/j.cemconres.2019.105824.

Chabaat, M., Thimus, J.F., et al., 2007. Use of scanning electron microscope and the non-local isotropic damage model to investigate fracture process zone in notched concrete beams. Experimental mechanics 47, 473–484.

Chateau, C., Nguyen, T.T., Bornert, M., Yvonnet, J., 2018. Dvc-based image subtraction to detect microcracking in lightweight concrete. Strain 54, e12276.

Fonseca, J., Bésuelle, P., Viggiani, G., 2013. Micromechanisms of inelastic deformation in sandstones: an insight using x-ray micro-tomography. Géotechnique Letters 3, 78–83.

Gabet, T., Malecot, Y., Daudeville, L., 2008. Triaxial behaviour of concrete under high stresses: Influence of the loading path on compaction and limit states. Cement and Concrete Research 38, 403–412.

Grédiac, M., Hild, F., 2013. Full-field measurements and identification in solid mechanics. Wiley Online Library.

Häfner, S., Eckardt, S., Luther, T., Könke, C., 2006. Mesoscale modeling of concrete: Geometry and numerics. Computers & structures 84, 450–461.

Hall, S., Bornert, M., Desrues, J., Pannier, Y., Lenoir, N., Viggiani, G., Bésuelle, P., 2010. Discrete and continuum experimental study of localised deformation in hostun sand under triaxial compression using x-ray μct and 3d digital image correlation. Géotechnique 60, 315–322.

Hild, F., Roux, S., 2012. Comparison of local and global approaches to digital image correlation. Experimental Mechanics 52, 1503–1519.

Huang, Y., Yang, Z., Ren, W., Liu, G., Zhang, C., 2015. 3d meso-scale fracture modelling and validation of concrete based on in-situ x-ray computed tomography images using damage plasticity model. International Journal of Solids and Structures 67, 340–352.

Hurley, R., Pagan, D., 2019. An in-situ study of stress evolution and fracture growth during compression of concrete. International Journal of Solids and Structures 168, 26–40.

Jia, Z., Shah, S.P., 1994. Two-dimensional electronic-speckle-pattern interferometry and concrete-fracture processes. Experimental Mechanics 34, 262–270.

Kim, S.M., Al-Rub, R.K.A., 2011. Meso-scale computational modeling of the plastic-damage response of cementitious composites. Cement and Concrete Research 41, 339–358.

Landis, E.N., Nagy, E.N., Keane, D.T., Nagy, G., 1999. Technique to measure 3d work-of-fracture of concrete in compression. Journal of engineering mechanics 125, 599–605.

Landis, E.N., Zhang, T., Nagy, E.N., Nagy, G., Franklin, W.R., 2007. Cracking, damage and fracture in four dimensions. Materials and Structures 40, 357–364.

Lucas, B.D., Kanade, T., et al., 1981. An iterative image registration technique with an application to stereo vision .

Malecot, Y., Zingg, L., Briffaut, M., Baroth, J., 2019. Influence of free water on concrete triaxial behavior: The effect of porosity. Cement and Concrete Research 120, 207–216.

Mao, L., Yuan, Z., Yang, M., Liu, H., Chiang, F.p., 2019. 3d strain evolution in concrete using in situ x-ray computed tomography testing and digital volumetric speckle photography. Measurement 133, 456–467.

Mehta, P.K., 1986. Concrete. structure, properties and materials .

Mindess, S., Diamond, S., 1980. A preliminary sem study of crack propagation in mortar. Cement and Concrete Research 10, 509–519.

Nemati, K.M., 1997. Fracture analysis of concrete using scanning electron microscopy. Scanning 19, 426–430.

Nitka, M., Tejchman, J., 2018. A three-dimensional meso-scale approach to concrete fracture based on combined dem with x-ray μct images. Cement and Concrete Research 107, 11–29.

Piotrowska, E., Malecot, Y., Ke, Y., 2014. Experimental investigation of the effect of coarse aggregate shape and composition on concrete triaxial behavior. Mechanics of Materials 79, 45–57.

Poinard, C., Malecot, Y., Daudeville, L., 2010. Damage of concrete in a very high stress state: experimental investigation. Materials and Structures 43, 15–29.

Poinard, C., Piotrowska, E., Malecot, Y., Daudeville, L., Landis, E.N., 2012. Compression triaxial behavior of concrete: the role of the mesostructure by analysis of x-ray tomographic images. European Journal of Environmental and Civil Engineering 16, s115–s136.

Reynouard, J.M., Pijaudier-Cabot, G., Torrenti, J.M., 2010. Mechanical behavior of concrete. Wiley, New-York.

Sfer, D., Carol, I., Gettu, R., Etse, G., 2002. Study of the behavior of concrete under triaxial compression. Journal of engineering mechanics 128, 156–163.

Stamati, O. Andò, E., Roubin, E., *et. al.*, C.R., 2020. spam: Software for practical analysis of materials. Submitted to Journal of Open Source Software 5, 2177.

Stamati, O., Roubin, E., Andò, E., Malecot, Y., 2019. Tensile failure of micro-concrete: from mechanical tests to fe meso-model with the help of x-ray tomography. Meccanica 54, 707–722.

Stamati, O., Roubin, E., Andò, E., Malecot, Y., 2018. Phase segmentation of concrete x-ray tomographic images at meso-scale: Validation with neutron tomography. Cement and Concrete Composites 88, 8 – 16. URL: http://www.sciencedirect.com/science/article/pii/S095894651730642X, doi:https://doi.org/10.1016/j.cemconcomp.2017.12.011.

Suchorzewski, J., Tejchman, J., Nitka, M., 2017. Discrete element method simulations of fracture in concrete under uniaxial compression based on its real internal structure. International Journal of Damage Mechanics , 1056789517690915.

Tudisco, E., Jailin, C., Mendoza, A., Tengattini, A., Andò, E., Hall, S.A., Viggiani, G., Hild, F., Roux, S., 2017. An extension of digital volume correlation for multimodality image registration. Measurement Science and Technology 28, 095401.

Vu, X.H., Daudeville, L., Malecot, Y., 2011. Effect of coarse aggregate size and cement paste volume on concrete behavior under high triaxial compression loading. Construction and Building Materials 25, 3941–3949. doi:10.1016/j.conbuildmat.2011.04.026.

Vu, X.H., Malecot, Y., Daudeville, L., 2009. Strain measurements on porous concrete samples for triaxial compression and extension tests under very high confinement. The Journal of Strain Analysis for Engineering Design 44, 633–657.

Weerheijm, J., 2013. Understanding the tensile properties of concrete. Elsevier.

Wriggers, P., Moftah, S., 2006. Mesoscale models for concrete: Homogenisation and damage behaviour. Finite elements in analysis and design 42, 623–636.

Yang, Z., Ren, W., Sharma, R., McDonald, S., Mostafavi, M., Vertyagina, Y., Marrow, T., 2017. In-situ x-ray computed tomography characterisation of 3d fracture evolution and image-based numerical homogenisation of concrete. Cement and Concrete Composites 75, 74–83.

Yu, Q., Liu, H., Yang, T., Liu, H., 2018. 3d numerical study on fracture process of concrete with different itz properties using x-ray computerized tomography. International Journal of Solids and Structures 147, 204 – 222. URL: http://www.sciencedirect.com/science/article/pii/S0020768318302208, doi:https://doi.org/10.1016/j.ijsolstr.2018.05.026.

Zingg, L., Briffaut, M., Baroth, J., Malecot, Y., 2016. Influence of cement matrix porosity on the triaxial behaviour of concrete. Cement and concrete research 80, 52–59.

Appendix A. Technical drawings of the 7075 T6 aluminium alloy cell

The design of this cell is based on an initial drawing done by Erminio Salvatore.

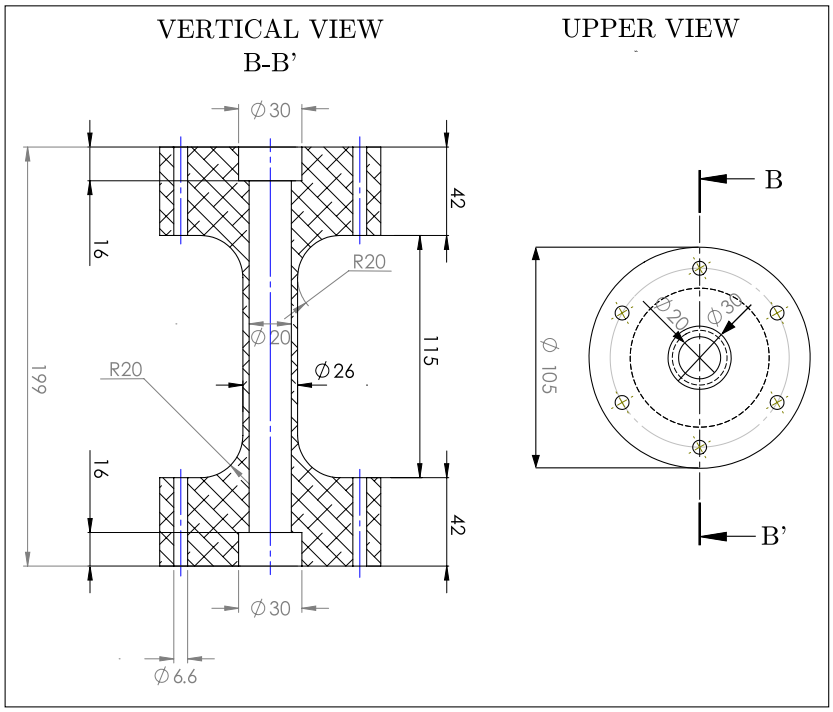

Figure A.16: Vertical and upper view of the cell

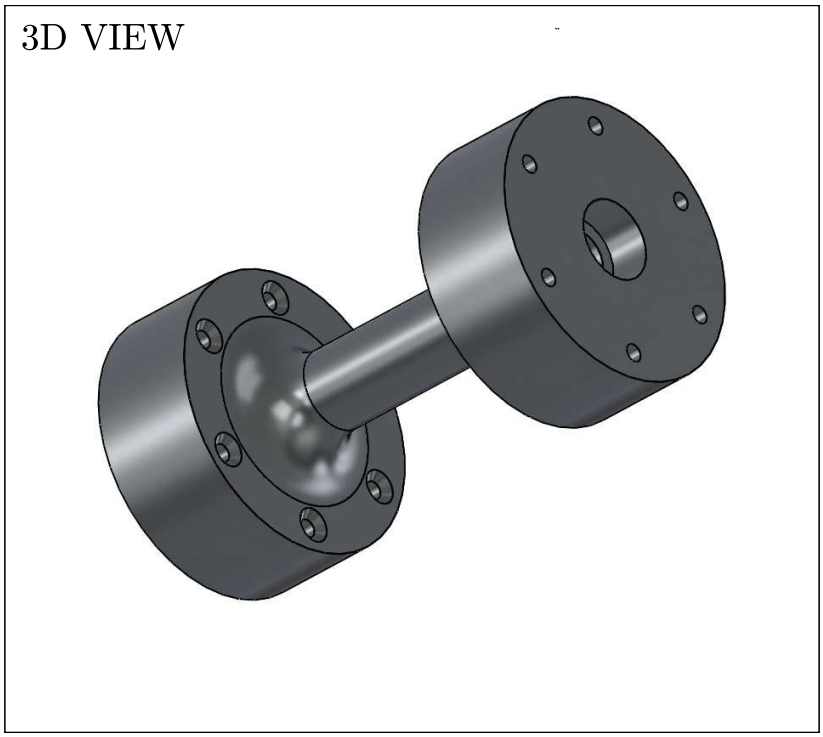

Figure A.17: 3D view of the cell

Appendix B. Uncertainty in measured elasticity modulus

The macroscopic Young's modulus based on a DVC displacement field is given by the following expression:

$$E = \frac{\sigma}{\epsilon} = \frac{FH}{Az} \tag{B.1}$$

where:

F: is the measured force level during the experiment,
A: is the measured surface area of the specimen,
z: is the difference between the measured displacements of the considered points and
H: is the initial distance between the two measurement points.

An estimation of the global error on the measured Young's modulus (ΔE) is given by the following expression:

$$\Delta E = \left|\frac{H}{Az}\right| \Delta F + \left|\frac{F}{Az}\right| \Delta H + \left|\frac{FH}{A^2 z}\right| \Delta A + \left|\frac{FH}{Az^2}\right| \Delta z \tag{B.2}$$

where:

ΔF: is the error in measuring the force during the experiment, as measured by the forcemeter, with a given by the manufacturer tolerance of 0.1 N,

ΔH: is the error in measuring the distance between two points in the image, which is of the magnitude of the voxel size and can be neglected,

ΔA: is the error in measuring the surface area of the specimen, which is given by: $A = \frac{\pi}{4} \times d^2$, so that $\Delta A = \frac{\pi}{2} \times d \times \Delta d$, where d is the diameter of the specimen and

Δz: is the error coming from the measured displacement field, which is the dominant one and is directly taken from the displacement uncertainty measured from the "repeated" scans (see Section 2.4.1).

Fig. B.18 depicts the measured Young's moduli, along with the corresponding error bars for both uniaxial (PMAA cell) and triaxial (aluminium cell) tests. The reference scan is correlated with the subsequent second one for a range of different window sizes. Starting from the bottom edge and traversing vertically the specimen, the axial displacements at each vertical grid position are averaged. Their relative difference (*i.e.*, z in Eq. B.1) is computed for a range of different vertical distances (*i.e.*, H in Eq. B.1) and the Young's moduli, with the corresponding error (see Eq. B.2) are computed for each window size.

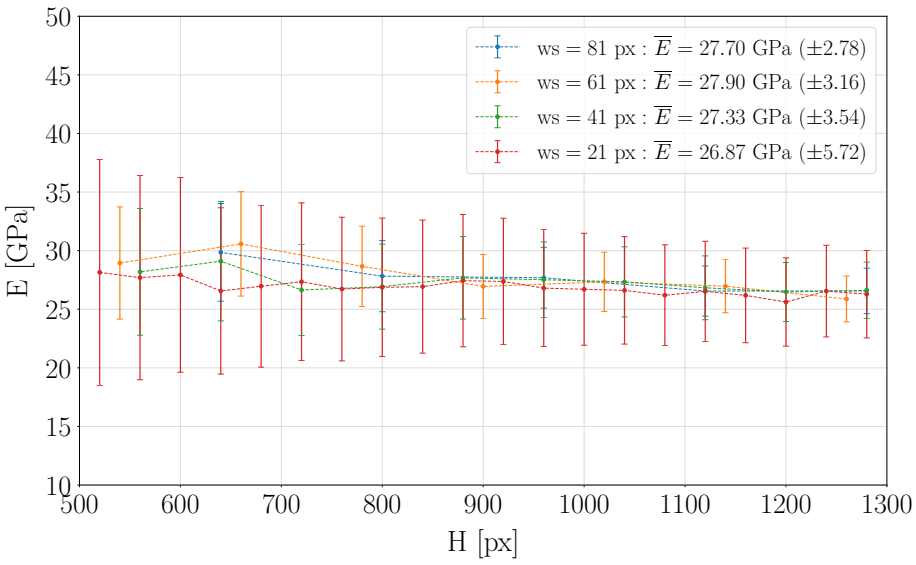

(a) C-02 test

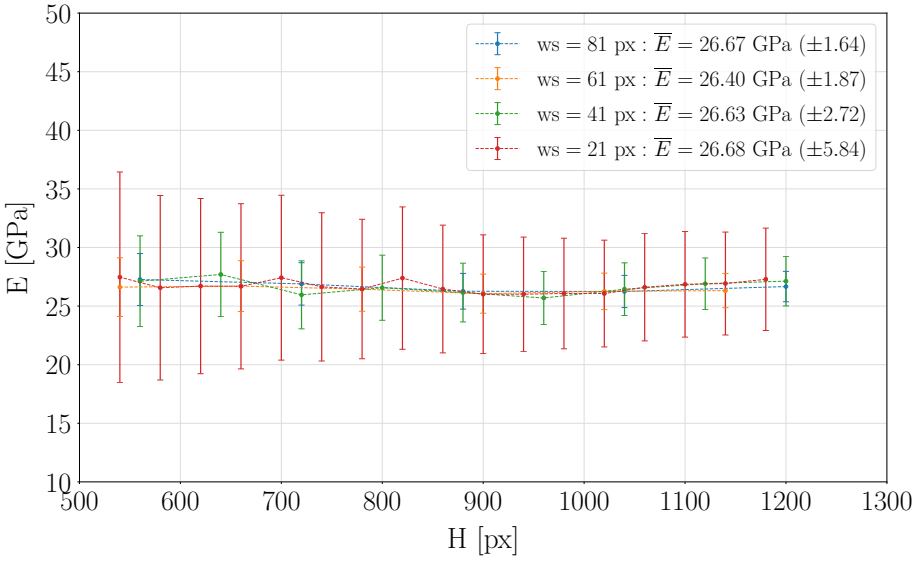

(b) TX15-01 test

Figure B.18: Estimation of DVC Young's moduli measurement uncertainties along the samples for uniaxial (PMAA cell) and triaxial (aluminium cell) tests for a range of correlation window sizes